Vibration Control in Cable Robots Using a Multi-Axis Reaction System

by

Mitchell Rushton

A thesis
presented to the University of Waterloo
in fulfillment of the
thesis requirement for the degree of
Master of Applied Science
in
Mechanical Engineering

Waterloo, Ontario, Canada, 2016

Author's Declaration

I hereby declare that I am the sole author of this thesis. This is a true copy of the thesis, including any required final revisions, as accepted by my examiners.

I understand that my thesis may be made electronically available to the public.

Abstract

The primary motivation of this thesis is to develop a control strategy for eliminating persistent vibrations in all six spatial directions of the end effector of a planar cable-driven parallel robotic manipulator.

By analysing the controllability of a cable-driven robot dynamic model, the uncontrollable modes of the robot are identified. For such uncontrollable modes, a new multi-axis reaction system (MARS) is developed. The new MARS that is attached to the end effector is made of two identical pendulums driven by two servo motors.

A decoupled PD controller strategy is developed for regulating controllable modes and a hierarchical sliding mode controller is developed for controlling the remaining modes of the cable robot using MARS. The performance of both controllers is studied and shown to be effective in simulation. The controllers are then implemented on an experimental test setup of a planar cable-driven manipulator. Both controllers are shown to completely eliminate the end effector vibrations.

Acknowledgments

I would like to greatly thank my supervisor, Prof. Amir Khajepour, for his guidance and continued support over the years.

I would like to acknowledge and thank lab technicians Jeff Graansma, Jeremy Reddekopp, and Kevin Cochran for their help maintaining the test setup and dealing with various problems that would arise. I would like to acknowledge and thank colleague Hamed Jamshidifar for our many discussions on the topics of cable-driven robots and for his help with lab testing and improving the test setup.

Finally, I would like to thank my family. I could not have completed this work without their caring and support.

Contents

List of Figures

List of Tables

Chapter 1

Introduction

1.1 Background

With the explosion of e-commerce in recent years, there is a strong need for high throughput automated warehousing solutions. A relatively new concept which has yet to be explored in industry is the use of large scale cable-driven parallel robotic manipulators for high speed pick and place operations. Cable driven manipulators contain a lot of advantages over traditional rigid link based alternatives. Cables are very light weight and flexible, allowing the manipulator to produce high accelerations, span large workspaces, and incur minimal setup and maintenance costs. The drawback of cable-driven systems however is that the elastic nature of the cables and more importantly their uni-directional load tolerance in only tensile forces results in low overall manipulator stiffness. The effect of this is end effector vibrations become a major obstacle for accurate positioning and control. This is perhaps the greatest hindrance preventing cable-driven parallel manipulators from gaining widespread use in industry. In particular for planar systems, where the translational stiffness in the planar normal direction is extremely low, this is a significant concern as any disturbances which excite the out of plane modes can lead to very large displacements of the end effector that cannot

be regulated by actuation of the cables.

For planar manipulators operating in confined spaces, such as a warehousing robot placed between two aisles, the consequences of unregulated end effector vibrations can have potentially catastrophic consequences if the displacements become large enough that a collision event occurs between the end effector and adjacent structures.

1.2 Objective and Contribution

The objective of this thesis is to develop and implement an active multi-axis vibration control system which is capable of attenuating undesired vibrations in all six spatial degrees of freedom for a fully-constrained planar cable driven parallel robot. All previous studies, that the author is aware of, on vibration control for planar systems have completely neglected the out of plane dynamics. Hence, the theoretical and supporting experimental work presented here is of significant value, especially in the applications of cable-driven or otherwise flexible robot manipulators for which the effects of low manipulator stiffness are a real hindrance for any practical industrial application.

The most significant contribution of this work is likely the theoretical analysis on using a set of inertial actuators, mounted at the end effector, for eliminating vibrations which occur along directions that are uncontrollable via cable actuation alone. Equally important, and perhaps even more so, is the actuator design presented in this work. It is shown that by using the proposed design, vibrations along the three axes which are uncontrollable via cable actuation can be eliminated with the addition of only two identical pendulum actuators.

1.3 Outline

Chapter 2 provides a survey of the existing literature in the field of cable driven robotics with a specific focus on elements relevant to vibration control.

Chapter 3 begins by presenting a spatial dynamic model for a planar cable-driven robot intended for warehousing type applications. A linearised version of the warehousing robot model is then used to identify the set of uncontrollable modes. A design for a reaction based damping system using two pendulum actuators is then presented and shown to make the system fully controllable, using a modified version of the previously presented warehousing robot model, updated to include the dynamics of the proposed damping mechanism.

Chapter 4 presents the developed control strategy for controlling the motion of the mobile platform and eliminating vibrations which may persist in any of the six spatial degrees of freedom. The effectiveness of the proposed control strategy is investigated in simulation.

Chapter 5 introduces the experimental setup used for verifying the simulation results of chapter 4. It also describes the design and construction of a pair of pendulum actuators and their necessary components.

In Chapter 6, experimental results are presented along with a related discussion.

Finally, chapter 7 includes a final discussion of the results obtained in this thesis. A brief summary of the work is presented and a set of final concluding marks are presented. Also included are a list of recommendations and suggestions for future works.

Chapter 2

Literature Review and Background

2.1 Cable Driven Parallel Robots

Cable driven parallel robots (CDPR) generally consist of a rigid mobile platform, which functions as the end effector, suspended by a number of elastic cables. The mobile platform is able to move through its workspace in a controlled maner by actuating the lengths of the individual cables. In recent decades, CDPRs have gained a lot of attention from robotic researchers [2, 3]. A likely reason for this is that CDPRs provide a number of significant advantages over traditional robotic manipulators which are based solely on rigid links.

In comparison to rigid links, cables are extremely light. This leads to CDPRs having very low inertia at the end effector, enabling them to command high accelerations and require less energy to operate. An excellent example for their potential in high-speed robotics is the FALCON robot which is able to travel at $14m/s$ and produce accelerations in excess of $40g$ [4]. A more industrial example is the DeltaBot, a cable based delta-robot, developed by Dekker and Khajepour, capable of performing 120 pick and place operations

per minute [5].

Because cables are light and their lengths are easily compactable by coiling, this enables CDPRs to span very large workspaces which would be impossible or unfeasible with a traditional manipulator. One application in which suspended CDPRs have been employed is large scale radio telescopes. The Arecibo radio telescope uses a CDPR with a span of over 300 meters to carry its 900 ton receiving platform 150m in the air [6]. The FAST radio telescope, which is currently under construction in China, uses a CDPR for the same purpose with a span of over $500m$ [7].

While the individual links of a traditional robotic manipulator typically have to be carefully designed and manufactured, cables are readily available and can be easily replaced or reconfigured. This enables the design of manipulators which are of lower cost and much easier to maintain than traditional manipulator designs.

Two main challenges inherent to CDPRs have been identified. First, and perhaps most significantly, is the fact that cables are only able to transmit force uniaxially and must be held under tension to do so. This makes the task of controlling CDPRs fairly challenging and requires a lot of addition considerations to ensure cable tensions are always maintained. Additionally, because cables are only able to apply forces uniaxially, this leads to a manipulator stiffness far lower than comparable rigid mechanisms. As a result of low manipulator stiffness, end effector vibrations are a serious hindrance to performance.

In the literature, CDPRs are divided into two main categories: under-constrained, and fully-constrained. Under-constrained CDPRs require an additional external force, such as gravity, in order for the robots motion to become fully constrained and produce the expected degrees of freedom. Fully-constrained CDPRs are redundantly actuated such that the robots motion is fully constrained using cable forces alone. Note: The redundancy condition is necessary for a CDPR to be fully-constrained using only cable forces because

of the fact that cables can only apply force uniaxially.

When modeling Cable driven mechanisms, typically the moving platform is assumed to be perfectly rigid because of its high relative stiffness. The interesting part of modeling comes when considering how to accurately include the effects of cables into both the kinematic and dynamic robot models. In the simplest case, cables are assumed as massless, straight line segments with no elongation. In more complicated studies, such effects as cable mass, sagging, and stretching are considered. While including the effects of cable mass and sagging does lead to a more realistic model, it also significantly increases the model complexity. Depending on the particular application, varying levels of model fidelity are applied successfully.

For fully constrained CDPRs, the cable internal tensile forces are typically much higher than that of the cable weight. In these cases, the massless and straight line assumptions work well and has been applied successfully in studies such as [8, 9, 10]. Conversely, for large suspended CDPRs, such as those used in large radio telescopes, cable mass and sagging has a much more significant effect and must be considered .

For studies which aim to investigate manipulator stiffness and vibration characteristics, cable elongation becomes necessary. This commonly involves representing cables as massless linear or nonlinear springs [11, 12, 13]. The effects of cable elongation are generally considered to be only significant in the axial direction. This assumption has long been shown to be effective in practical applications. Diao has provided theoretical support for this assumption in [14] where he shows that the effects of cable vibrations in the transversal direction do indeed contribute a negligible amount to overall cable vibrations and can reasonably be ignored.

The stiffness of a parallel manipulator largely contributes to its performance in terms of position control accuracy [15, 16]. This leads to one of the major drawbacks of CDPRs as the overall manipulator stiffness is relatively low due to the elastic nature of the cables. Comparatively, parallel

mechanisms built from rigid links are generally praised for their high stiffness relative to serial configurations.

Because of their high individual link stiffnesses, traditional parallel mechanisms can usually be assumed as perfectly rigid for purposes of control. Under this assumption, the end effector pose is kinematicly determined if joint positions are known. This leads to the first classification of position control methods: joint-space control. This control strategy involves commanding the manipulator joints to a particular desired configuration, determined by an inverse kinematics model. This approach has been adopted for cable-driven mechanisms in various studies [17, 18, 19]. It has been shown to work reasonably well for certain applications and is a viable solution if accelerations are low and the cables are relatively stiff.

As accelerations during a motion increase, the assumption of link rigidity no longer holds well and the effects of cable elongation start to become significant. In this state, the end effector is no longer kinematicly determinant, leading to errors in position during joint-space control. This leads to the requirement for a second method of position control: task-space control. In task space control, the aim is to control the end effector position directly, using direct measurement, and adjust the required joint positions as necessary. This approach has been applied to cable driven robots in several different studies [20, 21].

Due to the uniaxial property of cable forces, this requires fully-constrained CDPRs to be redundantly actuated. An n degree-of-freedom cable driven mechanism requires $\geq n + 1$ cables in order to be fully-constrained [22]. This leads to the condition where there are an infinite number of solutions for cable tensions. A common approach has been to solve this optimisation problem by the Jacobin pseudo-inverse method [23]. In [24], Hassan and Khajepour present a new method for solving the optimisation which results in a maximized manipulator stiffness.

Several studies have been performed to analyze the stiffness properties of

CDPRs. In [1] Méndez and Khajepour have analyzed the optimal locations of cables for maximising manipulator stiffness. In [16], Behzadipour and Khajepour have shown that the stiffness of a CDPR can always be improved by increasing the internal cable forces. While these efforts are valuable and do have an appreciable effect on reducing the impact of undesired vibrations, they are not a complete solution. Especially in the case of planar systems, where the out of plane stiffness is inherently very low [25].

A large number of studies have looked at active vibration control via cable actuation. For fully-constrained spatial mechanisms, where all six degrees of freedom corresponding to spatial motion are directly controllable using only internal forces, these efforts have proven to be an effective solution and can perform well at eliminating undesired vibrations. While this approach works well for fully-constrained spacial mechanisms, there remains two classes of CDPRs which still require special attention: under-constrained, and planar mechanisms.

Large scale suspended CDPRs are often subjected to external disturbances, such as wind, which combined with their scale, makes fine position control very difficult. In [26] as well as [27], the use of a secondary parallel mechanism, mounted at the mobile platform, is discussed as a method for improving fine positioning control of these types of systems. Gexue et al., in simulation, study the potential of using a 6-DOF Stewart platform attached at the mobile platform for the purposes of improving stability and vibration control in [28]. In [26], Sun et al. investigate the potential of using of a set of tuned mass dampers for the FAST radio telescope in simulation. Their initial results suggest that the adding of a set of tuned mass dampers to the mobile platform of a large scale suspended spatial CDPR can indeed help eliminate some of the effects of wind disturbances.

In most previous studies, such as [29, 30, 31], the effects of out of plane motions in planar CDPRs have been ignored. However, unless the mechanism is constrained, such that out of plane motions become impossible,

this assumption is not valid due to cable elongation. Méndez shows in [32] that manipulator out of plane stiffness is indeed very low, leading to major deflections in the face of disturbances.

For planar systems, control via cable acutation is an effective tool for eliminating spatial vibrations that lie within the plane. However, motions which lead the mobile platform away from its equilibrium plane remain uncontrolable and cannot be affected by cables alone. In [33], Weber, et al. investigate experimentally the use of reaction wheels for active damping of certain rotational modes for a two cable planar CPDR. In their study, they demonstrate that active inertia based damping techniques can produce positive results for CDPRs. However, they fail to consider out of plane translational motions which are by far the most significant problem for planar systems. The use of reaction wheels alone is insufficient for translational damping as they are not able to produce any force component to bring the mobile platform back to its equilibrium plane.

In the previous study of [34], Rushton and Khajepour investigated the optimal placement for an active sliding mass actuator to improve the controllability of a planar cable-driven robot. In that work it was shown that using an active sliding mass actuator oriented such that it is free to slide in and out of the plane can greatly improve the controllability for some of the out of plane modes and help regulate out of plane translational vibrations. This thesis takes that work further and investigates ways in which the problem of vibration control can be performed along all six spatial axes for a fully-constrained planar CDPR.

Chapter 3

Multi-Axis Reaction System for Vibration Control

From the perspective of motion planning and control, a planar manipulator consists of three degrees of freedom. Namely, translation about the two planar axes and a single rotation about the planar normal. In reality, it is possible for a manipulator to be displaced in all six spatial directions but this fact is generally ignored as the displacements in nonplanar dimensions are considered negligible. For many systems this assumption is fair and valid. If a manipulator is sufficiently stiff or otherwise constrained, such that the displacements caused by any anticipated disturbance forces are tolerable, out of plane dynamics can be ignored without any appreciable effect on the overall manipulator performance.

For systems that are not sufficiently stiff however, simply ignoring the out of plane dynamics can have potentially disastrous consequences. Consider a long span cable driven manipulator, intended for warehousing type applications. If the robot is installed between two aisles, there is a small tolerance for how much displacement the mobile platform can endure in the planar normal direction before there is a collision event with one of the adjacent aisles, resulting in damage to not only the robot, but also the warehouse

itself. In such cases, it is desirable or even necessary to have some method of regulating the mobile platform to ensure that it remains along its equilibrium plane.

This chapter begins by presenting a full spatial dynamic model for the cable driven warehousing robot under study. The controllability is then analyzed to identify the set of uncontrollable modes. Once this has been completed, a novel actuator design is presented which is capable of eliminating any persistent excitation of the uncontrollable modes.

The dynamic warehousing robot model is then updated to include the newly designed inertial actuators. Once again the controllability of the system is analyzed to demonstrate that with the addition of the proposed actuators, the system becomes fully controllable along all 6 spatial axes.

The chapter ends with a simulation study to demonstrate the capabilities of the actuators at suppressing the uncontrollable modes and to provide some insight into the system behavior.

3.1 Warehousing Robot Dynamic Model

The system consists of a mobile platform suspended by twelve cables. Figure 3.1 shows the geometric configuration of the robot and location of the cable mount points. Though the system has twelve cables, it is driven by only four actuators. A single motor is present in each of the four corners of the fixed frame. Each motor is responsible for driving multiple cables. The locations of the cable mount points are selected such that the unstretched lengths for all cables driven by the same motor are equivalent. The justification for adding the additional redundant cables is that it helps to improve the overall manipulator stiffness without requiring any additional control complexity. For more discussion on the details of the manipulator design and how those particular mount point locations were obtained, the reader is referred to [32].

It is assumed in this model that the unstretched length of the cables are

directly controllable by the motors. A full spatial dynamic model representing the dynamics of a cable driven manipulator, such as the one in Figure 3.1, will be developed in the proceeding sub sections.

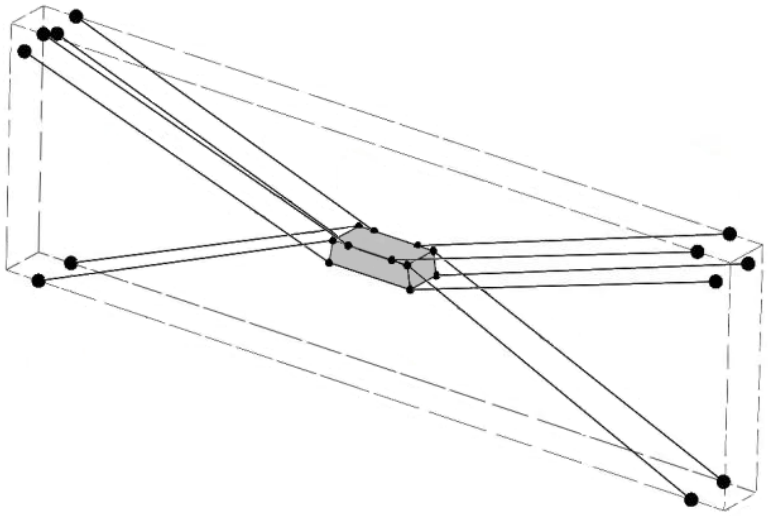

Figure 3.1: Warehousing robot cable configuration [1]

3.1.1 Rotations and Frames

There exists a ground fixed inertial frame, g, and a body-fixed frame, b. The ground fixed frame is oriented such the x axis is horizontal, the y axis points in the positive vertical direction, and the z axis points out of the plane. The origin is placed at the centre of the workspace. The body-fixed frame is attached to the center of mass of the mobile platform and oriented along the platform's principal axes of inertia (see Figure 3.3) such that I_p, the inertia tensor for the platform, becomes:

$$I_p = \begin{bmatrix} I_{xx} & 0 & 0 \\ 0 & I_{yy} & 0 \\ 0 & 0 & I_{zz} \end{bmatrix} \tag{3.1}$$

The orientation of the platform with respect to the ground is defined using $[1, 2, 3]$ body-fixed Euler angles. Using this convention, the rotation matrix from the ground frame to the body-fixed frame is found as:

$$R_g^b = R_z(\phi)R_y(\theta)R_x(\psi) \tag{3.2}$$

where ψ, θ, and ϕ are the rotations about the global x, y', and z'' axes respectively. While the existence of singularities is an inherent problem with the use of Euler angles, for the type of mechanism analyzed in this thesis, they are deemed sufficient. The singularity is reached when $\theta = \pm 90°$. Given the physical constraints, a singular configuration is not realistically achievable.

The pose of the platform at a particular point in time is defined by two vectors, p and q, which track the position and orientation of the platform respectively.

$$p = \begin{bmatrix} x \\ y \\ z \end{bmatrix}, \quad q = \begin{bmatrix} \psi \\ \theta \\ \phi \end{bmatrix} \tag{3.3}$$

Since it is desired to eventually form the system equations in terms of the Euler angles and Euler angle rates, it is necessary to provide a relation between the Euler angle rates and the angular velocity of the platform. The necessary transformation can be found by projecting $\dot{q}$ onto the body-fixed axes.

$$\begin{gathered} \omega = \dot{\psi}\hat{i} + \dot{\theta}\hat{j}' + \dot{\phi}\hat{k}'' \\ \begin{bmatrix} \omega_x \\ \omega_y \\ \omega_z \end{bmatrix} = R_g^b \begin{bmatrix} \dot{\psi} \\ 0 \\ 0 \end{bmatrix} + R_{''}^b R_{'}'' \begin{bmatrix} 0 \\ \dot{\theta} \\ 0 \end{bmatrix} + \begin{bmatrix} 0 \\ 0 \\ \dot{\phi} \end{bmatrix} \end{gathered} \tag{3.4}$$

Simplifying (3.4), the following transformation matrix, R_r can be obtained for relating ω and $\dot{q}$:

$$\omega = R_r \dot{q} = \begin{bmatrix} \cos(\phi)\cos(\theta) & \sin(\phi) & 0 \\ -\cos(\theta)\sin(\phi) & \cos(\phi) & 0 \\ \sin(\theta) & 0 & 1 \end{bmatrix} \begin{bmatrix} \dot{\psi} \\ \dot{\theta} \\ \dot{\phi} \end{bmatrix} \tag{3.5}$$

The relation between $\dot{\omega}$ and $\ddot{q}$ can be found by differentiating (3.5) with respect to time.

3.1.2 Single Cable Model

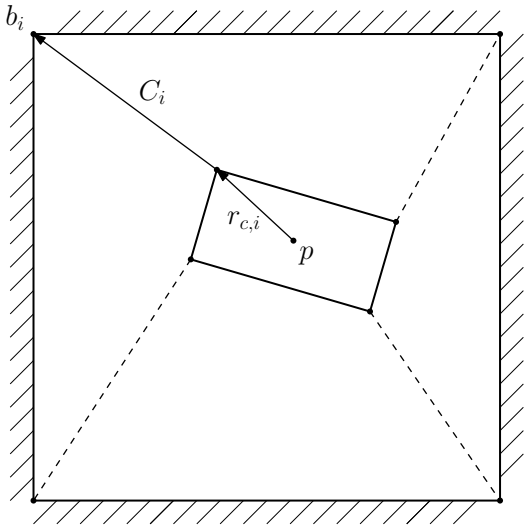

Figure 3.2: Cable mount points and length vector

Each of the n cables have two mount points: one fixed to the frame and one fixed to the body (see Figure 3.2). For a particular cable, i, and a particular robot pose, $\{p, q\}$, the vector formed between the two mounts in the ground frame, C_i, is determined by the following geometric relation:

$$C_i = b_i - (p + R_b^g r_{c,i}) \tag{3.6}$$

where $r_{c,i}$ is the location of the body-fixed mount in the body-fixed frame and b_i is the location of the ground fixed mount in the ground frame. The

length of cable i is then simply the magnitude of vector C_i. Unit vector $\hat{c}_i$ points in the direction from the platform to the ground fixed mount along the length of the cable.

$$\hat{c}_i = \frac{C_i}{\|C_i\|}, \quad l_i = \|C_i\| \tag{3.7}$$

Each cable is modelled as a massless linear spring with a particular stiffness k_i. Given the current length of a cable, l_i, and its unstretched length, δl_i, the tension in the cable can be found as:

$$\tau_i = k_i(l_i - \delta l_i) \tag{3.8}$$

3.1.3 Spatial Dynamics of the Mobile Platform

Using the cable force model defined in the previous section, it is possible to define the complete spatial dynamics for the mobile platform. The resulting force and moment produced by the ith cable from the perspective of the platform is found as:

$$F_i = \tau_i \hat{c}_i, \quad M_i = r_{c,i} \times (R_g^b F_i) \tag{3.9}$$

where F_i is in the ground frame and M_i is in the body-fixed frame. Note: the transformation of F_i from the ground frame to the body-fixed frame is necessary since the rotational accelerations are to be calculated in the body-fixed frame.

Summing the forces and moments produced by the individual cables, the total net force and moment applied to the platform are found to be:

$$F_c = \sum_{i=1}^{n} F_i, \quad M_c = \sum_{i=1}^{n} M_i \tag{3.10}$$

Then, using the Newton-Euler equations of motion, the spatial dynamics of the platform are defined as:

$$\begin{aligned} M_p\ddot{p} &= F_c + m_p\, g, \\ I_p\dot{\omega} &= M_c - \omega \times (I_p\omega) \end{aligned} \tag{3.11}$$

where m_p is the mass of the platform, g is the gravitational acceleration vector, and M_p is the mass matrix associated with the mobile box and is defined as:

$$M_p = \begin{bmatrix} m_p & 0 & 0 \\ 0 & m_p & 0 \\ 0 & 0 & m_p \end{bmatrix} \tag{3.12}$$

(3.11) can then be made in terms of Euler angles by using the transformations outlined in section 3.1.1. This results in the following alternative representation:

$$\begin{aligned} I_p\left(\dot{R}_r\dot{q} + R_r\ddot{q}\right) &= M_c - (I_bR_r\dot{q}) \times (I_bR_r\dot{q}) \\ R_r\ddot{q} &= I_p^{-1}\left[M_c - (R_r\dot{q}) \times (I_bR_r\dot{q})\right] - \dot{R}_r\dot{q} \\ \ddot{q} &= R_r^{-1}\left[I_p^{-1}\left(M_c - (R_r\dot{q}) \times (I_bR_r\dot{q})\right) - \dot{R}_r\dot{q}\right] \end{aligned} \tag{3.13}$$

3.2 Controllability Analysis

The dynamic equations of (3.11), derived in Section 3.1, can be rearranged to fit the following form:

$$\begin{aligned} \ddot{p} &= M_p^{-1}\left(F_c + m_p\, g\right) \\ \ddot{q} &= R_r^{-1}\left[I_p^{-1}\left(M_c - (R_r\dot{q}) \times (I_bR_r\dot{q})\right) - \dot{R}_r\dot{q}\right] \end{aligned} \tag{3.14}$$

The state variables required to represent the system consist of the platform position, orientation, and their first rates. The system inputs consist

of the unstretched lengths of the driven cables. This leads to the following definitions for the state and input vectors:

$$X = \begin{bmatrix} p \\ \dot{p} \\ q \\ \dot{q} \end{bmatrix}, \quad u = \begin{bmatrix} \delta l_1 \\ \delta l_2 \\ \delta l_3 \\ \delta l_4 \end{bmatrix} \tag{3.15}$$

where X and u are the state and input vectors respectively. Using (3.14) and (3.15), the following nonlinear state space model can is defined:

$$\dot{X} = \begin{bmatrix} \dot{p} \\ M_p^{-1}\left(F_c + m_p\, g\right) \\ \dot{q} \\ R_r^{-1}\left[I_p^{-1}\left(M_c - (R_r\dot{q}) \times (I_b R_r \dot{q})\right) - \dot{R}_r\dot{q}\right] \end{bmatrix} \tag{3.16}$$

where F_c and M_c are functions of p, q, and u. Once the system has been put into the form of (3.16), it can then be linearised using Taylor series expansion about an equilibrium point. Any location within the plane can be used as a potential equilibrium point so long as the elements of u are chosen such that the cable tensions hold the platform in a state of static equilibrium.

The equations of (3.16) were generated symbolically using a Matlab script which makes use of the Matlab symbolic toolbox. For the complete Matlab code used to generate and linearise system (3.16), The reader can refer to Appendix A

The locations for the cable mountpoints used in the model are the same as those presented in Table 5.1 on page 60. The remaining parameters used for generating the equations are presented in Table 3.1. Linearising about the equilibrium point $X = 0_{12\times1}$, $u = [0.5924, 0.5924, 0.5686, 0.5686]^T$, the following linear state space model is obtained:

$$\dot{X} = A_{12\times12}X + B_{12\times4}u \tag{3.17}$$

Table 3.1: Warehousing robot model parameters

Parameter	Value
m_p	$10\,kg$
I_p	$\begin{bmatrix} 0.0218 & 0 & 0 \\ 0 & 0.1187 & 0 \\ 0 & 0 & 0.1251 \end{bmatrix}\ Kg \cdot m^2$
k_c	$100\,N/m$

where matrices A and B are defined as:

$$A = \begin{bmatrix} 0 & 0 & 0 & 1.0 & 0 & 0 & 0 & 0 & 0 & 0 & 0 & 0 \\ 0 & 0 & 0 & 0 & 1.0 & 0 & 0 & 0 & 0 & 0 & 0 & 0 \\ 0 & 0 & 0 & 0 & 0 & 1.0 & 0 & 0 & 0 & 0 & 0 & 0 \\ -114.0 & 0 & 0 & 0 & 0 & 0 & 0 & 0 & -1.35 & 0 & 0 & 0 \\ 0 & -75.5 & 0 & 0 & 0 & 0 & 0 & 0 & 0 & 0 & 0 & 0 \\ 0 & 0 & -70.2 & 0 & 0 & 0 & 0.416 & 0 & 0 & 0 & 0 & 0 \\ 0 & 0 & 0 & 0 & 0 & 0 & 0 & 0 & 0 & 1.0 & 0 & 0 \\ 0 & 0 & 0 & 0 & 0 & 0 & 0 & 0 & 0 & 0 & 1.0 & 0 \\ 0 & 0 & 0 & 0 & 0 & 0 & 0 & 0 & 0 & 0 & 0 & 1.0 \\ 0 & 0 & 191.0 & 0 & 0 & 0 & -153.0 & 0 & 0 & 0 & 0 & 0 \\ 0 & 0 & 0 & 0 & 0 & 0 & 0 & -1866.0 & 0 & 0 & 0 & 0 \\ -108.0 & 0 & 0 & 0 & 0 & 0 & 0 & 0 & -1799.0 & 0 & 0 & 0 \end{bmatrix} \tag{3.18}$$

$$B = \begin{bmatrix} 0 & 0 & 0 & 0 \\ 0 & 0 & 0 & 0 \\ 0 & 0 & 0 & 0 \\ 37.9 & -37.9 & 18.7 & -18.7 \\ -12.7 & -12.7 & 7.06 & 7.06 \\ 0 & 0 & 0 & 0 \\ 0 & 0 & 0 & 0 \\ 0 & 0 & 0 & 0 \\ 0 & 0 & 0 & 0 \\ 0 & 0 & 0 & 0 \\ 0 & 0 & 0 & 0 \\ 196.0 & -196.0 & -100.0 & 100.0 \end{bmatrix} \tag{3.19}$$

The controllability of system (3.17) can be assessed by taking the rank of the controllability matrix, Q, which is defined as:

$$Q = \begin{bmatrix} B & AB & A^2B & \cdots & A^{n-1}B \end{bmatrix} \tag{3.20}$$

Evaluating the rank of Q, it can be seen that six of the twelve modes are uncontrollable and therefore, an additional set of actuators is required in order to eliminate any persistent excitation of the uncontrollable modes. By investigating the form of A and B, it is observed that the input has no effect on the state variables corresponding to out of plane motions. Specifically: $\psi,\ \dot{\psi},\ \theta,\ \dot{\theta},\ z,$ and $\dot{z}$.

3.3 Inertial Actuator Design

One potential actuator design approach capable of producing the required set of moments and forces to affect the uncontrollable modes, identified in Section 3.2, is the use of an inertia based reactionary mechanism. The basic concept is to add an additional inertial load to the mobile platform. Any forces applied to such a load will also generate and equal and opposite reaction force on the platform. This concept has been employed widely in the form of reaction wheels, an inertial disk used for attitude control of satellites, and as well with tuned mass dampers, employed in skyscrapers for eliminating structural vibrations induced by disturbances such as wind.

In order to dampen vibrations along the uncontrollable axes, such an actuator would be need to be able to produce a moment along the body-fixed x and y axes, as well as a force along the body-fixed z axis. Perhaps the most obvious solution would be to add two reaction wheels, one along each of the x and y axes, and a single tuned mass damper, aligned to oscillate along the z axis. While this would solve the controllability problem, it is not necessarily the best design solution in terms of cost or simplicity or performance.

Consider instead, a rigid pendulum coupled to the shaft of a motor which is mounted at some location on the mobile platform (see Figure 3.3). Due to the unbalanced nature of the pendulum shaped load mass, an applied torque along the motor shaft will produce a corresponding reaction torque, as well as a reaction force which is tangential to the position of the pendulum along its arc of motion. Depending on where the actuator is mounted on the platform, the reaction force from the pendulum will also produce a secondary set of reaction moments, due the displacement of the force from the various rotational axes.

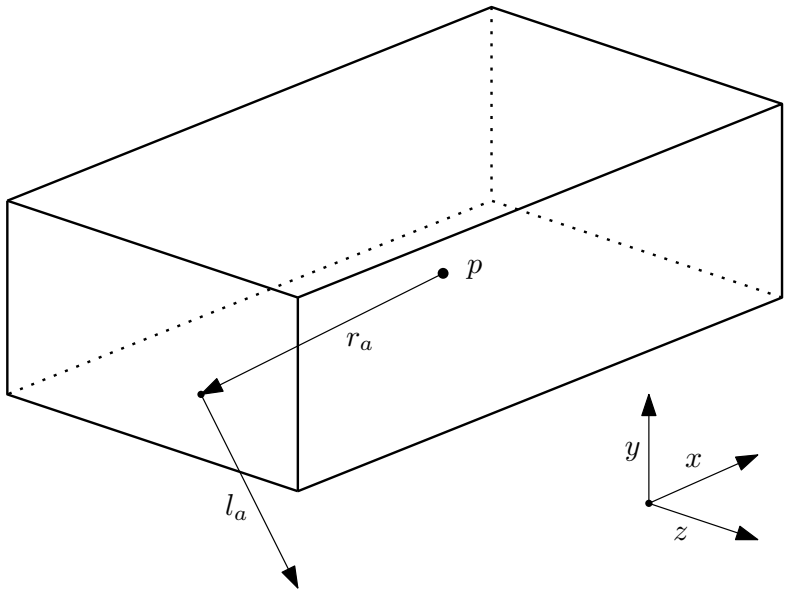

Figure 3.3: Pendulum load and defining geometry terms

A pendulum consists of a single rigid link which is free at one end and at the other end, attached to another body via a revolute joint. The kinematics of a pendulum mounted to the platform are defined by two vectors expressed in the body-fixed frame: the position of the revolute joint relative to the platform centre of mass, and the position of the pendulum centre of mass relative to the revolute joint. These two vectors are labeled as r_a and l_a

respectively.

For a single pendulum added to the mobile platform and mounted such that the pendulum is free to rotate along the x axis, any torque applied along the motor shaft, τ_a, will also generate the following reaction force and moments:

$$\begin{aligned} F_z &= -\tau_a \times l_a \\ M_x &= -\tau_a + \left[\left(r_a \cdot \hat{j}\right) \times F_z\right] \\ M_y &= \left(r_a \cdot \hat{i}\right) \times F_z \end{aligned} \tag{3.21}$$

where $\hat{i}$ and $\hat{j}$ are aligned with the x and y axes respectively. For the sake of robustness, it can noted from observing (3.21) that as long as the centre of mass remains above the pendulum mount point, the sign of the x moment produced by F_z will remain the same.

It is worth mentioning at this time that there is an inherent coupling in the dynamics of z and ψ. This coupling can be observed by examining the A matrix of (3.17). With a single pendulum, assuming it is mounted along the z axis such that M_y becomes zero, a coupled force moment pair is generated by the applied torque, τ_a. Exploiting the inherent coupling between the z and θ_x dynamics, both can be controlled simultaneously via the coupled F_z, M_x reaction pair.

Adding a second equivalent pendulum and mounting the pair of actuators such they are mirrored about z, y plane, it becomes possible to produce a pure moment about the y axis while still maintaining the ability to produce the coupled force moment pair of the single pendulum case.

If $\tau_{a,1}$ and $\tau_{a,2}$, the motor torques applied to the two respective pendulums, are equal, the y moments generated by each pendulum will be equal in magnitude but opposite in sign. Summing the two reaction y moments will result in a net zero moment being applied to the platform. Additionally,

the moment-force reaction pair generated by each pendulum will be equal in both sign and magnitude, thus the resulting reaction pair will be twice that of the reaction pair generated by a single pendulum.

If $\tau_{a,1}$ and $\tau_{a,2}$ are equal in magnitude but opposite in sign, the reaction moment-force pairs will also be equal in magnitude but opposite in sign. In this case, the signs of the two reaction moments in the y direction will be equal in sign, thus leading to a nonzero net moment being applied to the platform. At the same time, the x moment and z forces applied by the two pendulums will cancel each other out.

Depending on the signs of the motor torques applied to pendulums, it is therefore shown to be possible to generate a pure moment in the y direction or a coupled force-moment pair independently. Thus with the addition of two identical inertia based actuators, reaction forces can be generated to affect the three uncontrollable modes of the platform spatial dynamics.

3.4 Pendulum Dynamic Modeling

For deriving the model of the warehousing robot with two attached pendulum actuators, Lagrangian mechanics will be used as it simplifies the analysis when confronted with the reactions of between the pendulums and the platform. The kinetic energy and potential energy of the platform, T_p and V_p respectively, are defined as:

$$\begin{aligned} T_p &= \frac{1}{2} m_p \left(\dot{p} \cdot \dot{p}\right) + \frac{1}{2} \omega^T I_p \omega \\ V_p &= m_p \vec{g} \left(p \cdot \hat{j}\right) \end{aligned} \tag{3.22}$$

Using the cable model described in Section 3.1.2, the potential energy for the ith cable can be found as:

$$V_{c,i} = \frac{1}{2} k_i (l_i - \delta l_i)^2 \tag{3.23}$$

The kinetic energy and gravitational potential energy terms for the cables are zero since they are assumed to be massless. In order to define the kinetic and potential energy terms for each of the i pendulum actuators, it is first necessary to obtain an expression of their rotational and translation velocities. Consider the platform mounted pendulum of Figure 3.3. The location of the centre of mass of the ith pendulum, with respect to the ground, is found to be:

$$p_{a,i} = p + R_b^g \left(r_{a,i} + l_{a,i} \right) \tag{3.24}$$

Taking the time derivative of (3.24), the pendulum velocity is then:

$$\dot{p}_{a,i} = \dot{p} + R_b^g \left[(\omega_p \times r_{a,i}) + (\omega_{a,i} \times l_{a,i}) \right] \tag{3.25}$$

The angular velocity is simply the sum of the angular velocity of the pendulum about its revolute joint, $\dot{\theta}_{a,i}$, with the angular velocity of the platform. Namely:

$$\omega_{a,i} = \omega + \dot{\theta}_{a,i} \tag{3.26}$$

With the use of (3.24), (3.25), and (3.26), the kinetic energy for the ith pendulum is defined as:

$$T_{a,i} = \frac{1}{2} m_{a,i} \left(\dot{p}_{a,i} \cdot \dot{p}_{a,i} \right) + \frac{1}{2} \omega_{a,i}^T \, I_{a,i} \, \omega_{a,i} \tag{3.27}$$

and the potential energy for the ith pendulum:

$$V_{a,i} = m_{a,i} \ \left(g \cdot p_{a,i} \right) \tag{3.28}$$

Now that all of the energy terms have been computed, the Lagrangian can be formed as:

$$\mathcal{L} = (T_p + T_{a,1} + T_{a,2}) - \left(V_p + \sum_{i=1}^{n} V_{c,i} + V_{a,1} + V_{a,2} \right) \tag{3.29}$$

The Euler-Lagrange equations for the state variables associated with the mobile platform and the two pendulums become:

$$\begin{aligned}
\frac{d}{dt}\left\{\frac{\partial \mathcal{L}}{\partial \dot{p}}\right\} - \frac{\partial \mathcal{L}}{\partial p} &= 0 \\
\frac{d}{dt}\left\{\frac{\partial \mathcal{L}}{\partial \dot{q}}\right\} - \frac{\partial \mathcal{L}}{\partial q} &= 0 \\
\frac{d}{dt}\left\{\frac{\partial \mathcal{L}}{\partial \dot{\theta}_{a,1}}\right\} - \frac{\partial \mathcal{L}}{\partial \theta_{a,1}} &= \tau_{a,1} \\
\frac{d}{dt}\left\{\frac{\partial \mathcal{L}}{\partial \dot{\theta}_{a,2}}\right\} - \frac{\partial \mathcal{L}}{\partial \theta_{a,2}} &= \tau_{a,2}
\end{aligned} \tag{3.30}$$

where $\tau_{a,1}$ and $\tau_{a,2}$ are the applied torques for the two pendulums. As in Section 3.1, the equations of (3.30) are solved for and linearised by the use of a Matlab script. The code used for generating the model is provided in Appendix A. The model parameters relevant to the warehousing robot are the same as in Section 3.1. Table 3.2 contains the values used for the additional parameters required to describe the pendulums.

To accommodate the states and control inputs added by the two pendulums, the state and input vectors, X and u, must be updated as follows:

Table 3.2: Pendulum model parameters

Parameter	Value
$m_{a,i}$	$0.6\,kg$
$I_{a,i}$	$\begin{bmatrix} 655 & 0 & 0 \\ 0 & 483 & 0 \\ 0 & 0 & 191 \end{bmatrix} Kg \cdot mm^2$
$r_{a,1}$	$\begin{bmatrix} 0.2325, -0.0480, 0 \end{bmatrix}^T m$
$r_{a,2}$	$\begin{bmatrix} -0.2325, -0.0480, 0 \end{bmatrix}^T m$
$l_{a,i}$	$\begin{bmatrix} 0, -0.05, 0 \end{bmatrix}^T m$

$$X = \begin{bmatrix} p \\ \dot{p} \\ q \\ \dot{q} \\ \theta_{a,1} \\ \dot{\theta}_{a,1} \\ \theta_{a,2} \\ \dot{\theta}_{a,2} \end{bmatrix}, u = \begin{bmatrix} \delta l_1 \\ \delta l_2 \\ \delta l_3 \\ \delta l_4 \\ \tau_{a,1} \\ \tau_{a,2} \end{bmatrix} \tag{3.31}$$

After solving (3.30) for $\dot{X}$, the dynamic equations can be linearised using Taylor series expansion. Doing so about the equilibrium point $X = 0_{16\times1}$, $u = [0.5461, 0.5461, 0.5686, 0.5686, 0, 0]^T$, the following linear state space model is obtained:

$$\dot{X} = A_{16\times16}X + B_{16\times6}u \tag{3.32}$$

where matrices A and B are defined as:

$$A_{1:16\times1:9} = \begin{bmatrix} 0 & 0 & 0 & 1.0 & 0 & 0 & 0 & 0 & 0 \\ 0 & 0 & 0 & 0 & 1.0 & 0 & 0 & 0 & 0 \\ 0 & 0 & 0 & 0 & 0 & 1.0 & 0 & 0 & 0 \\ -102.0 & 0 & 0 & 0 & 0 & 0 & 0 & 0 & 5.11 \\ 0 & -69.5 & 0 & 0 & 0 & 0 & 0 & 0 & 0 \\ 0 & 0 & -70.0 & 0 & 0 & 0 & -0.982 & 0 & 0 \\ 0 & 0 & 0 & 0 & 0 & 0 & 0 & 0 & 0 \\ 0 & 0 & 0 & 0 & 0 & 0 & 0 & 0 & 0 \\ 0 & 0 & 0 & 0 & 0 & 0 & 0 & 0 & 0 \\ 0 & 0 & 66.0 & 0 & 0 & 0 & -172.0 & 0 & 0 \\ 0 & 0 & 0 & 0 & 0 & 0 & 0 & -1633.0 & 0 \\ -31.9 & 0 & 0 & 0 & 0 & 0 & 0 & 0 & -1200.0 \\ 0 & 0 & 0 & 0 & 0 & 0 & 0 & 0 & 0 \\ 0 & 0 & 999.0 & 0 & 0 & 0 & 87.5 & -5299.0 & 0 \\ 0 & 0 & 0 & 0 & 0 & 0 & 0 & 0 & 0 \\ 0 & 0 & 999.0 & 0 & 0 & 0 & 87.5 & 5299.0 & 0 \end{bmatrix}$$

$$A_{1:16\times10:16} = \begin{bmatrix} 0 & 0 & 0 & 0 & 0 & 0 & 0 \\ 0 & 0 & 0 & 0 & 0 & 0 & 0 \\ 0 & 0 & 0 & 0 & 0 & 0 & 0 \\ 0 & 0 & 0 & 0 & 0 & 0 & 0 \\ 0 & 0 & 0 & 0 & 0 & 0 & 0 \\ 0 & 0 & 0 & 0.423 & 0 & 0.423 & 0 \\ 1.0 & 0 & 0 & 0 & 0 & 0 & 0 \\ 0 & 1.0 & 0 & 0 & 0 & 0 & 0 \\ 0 & 0 & 1.0 & 0 & 0 & 0 & 0 \\ 0 & 0 & 0 & 8.0 & 0 & 8.0 & 0 \\ 0 & 0 & 0 & -6.83 & 0 & 6.83 & 0 \\ 0 & 0 & 0 & 0 & 0 & 0 & 0 \\ 0 & 0 & 0 & 0 & 1.0 & 0 & 0 \\ 0 & 0 & 0 & -162.0 & 0 & 19.1 & 0 \\ 0 & 0 & 0 & 0 & 0 & 0 & 1.0 \\ 0 & 0 & 0 & 19.1 & 0 & -162.0 & 0 \end{bmatrix} \tag{3.33}$$

$$B = \begin{bmatrix} 0 & 0 & 0 & 0 & 0 & 0 \\ 0 & 0 & 0 & 0 & 0 & 0 \\ 0 & 0 & 0 & 0 & 0 & 0 \\ 33.2 & -33.2 & 17.0 & -17.0 & 0 & 0 \\ -11.3 & -11.3 & 6.3 & 6.3 & 0 & 0 \\ 0 & 0 & 0 & 0 & -1.44 & -1.44 \\ 0 & 0 & 0 & 0 & 0 & 0 \\ 0 & 0 & 0 & 0 & 0 & 0 \\ 0 & 0 & 0 & 0 & 0 & 0 \\ 0 & 0 & 0 & 0 & -27.2 & -27.2 \\ 0 & 0 & 0 & 0 & 23.2 & -23.2 \\ 117.0 & -117.0 & -70.0 & 70.0 & 0 & 0 \\ 0 & 0 & 0 & 0 & 0 & 0 \\ 0 & 0 & 0 & 0 & 549.0 & -65.1 \\ 0 & 0 & 0 & 0 & 0 & 0 \\ 0 & 0 & 0 & 0 & -65.1 & 549.0 \end{bmatrix} \tag{3.34}$$

Once again the system controllability is analyzed using the same method as Section 3.2. After completing such analysis, it can be observed that by adding two of pendulum actuators, proposed in Section 3.3, the controllability matrix Q becomes full rank and therefore, at least locally, the system becomes fully controllable.

3.5 Simulation of Linearised Models

Using the linearised form of the models defined in Sections 3.1 and 3.4 a brief simulation study has been performed to demonstrate the capabilities of using a set of two pendulum actuators for eliminating persistent excitation of the uncontrollable modes the analyzed warehousing robot.

Three different test cases are considered. In each case, the mobile platform is given some initial condition and allowed to oscillate freely thereafter. State space models of the warehousing robot with and without the duel pendulum actuators are simulated side by side to demonstrate the regulation performance of the proposed actuators. The pendulums are controlled

through the use of a Linear Quadratic Regulator (LQR). The same designed LQR is used for all three cases.

The simulated system response for test cases 1-3 are presented in Figures 3.4, 3.5, and 3.6 respectively. For the system without the pendulum actuators, in all three test cases, the platform oscillates indefinably without any attenuation. This result is expected since the model contains no natural damping.

Figure 3.4 shows how the system is able to eliminate oscillations in the z and θ_x directions simultaneously. The natural frequency of the θ_x dynamics are significantly higher than that of z. Very quickly, the high frequency oscillations of θ_x are eliminated leaving only the lower frequency content resulting from the out of plane translational mode to be slowly attenuated with time.

Figure 3.5 focuses fully on the potential for the duel pendulum system at regulating θ_y. As predicated, by swinging the pendulums in opposite directions, θ_y can be regulated without any undesired excitation of the z and θ_x modes.

In Figure 3.6, It is demonstrated that the duel pendulum actuators are capable of regulating z, θ_x, and θ_y simultaneously.

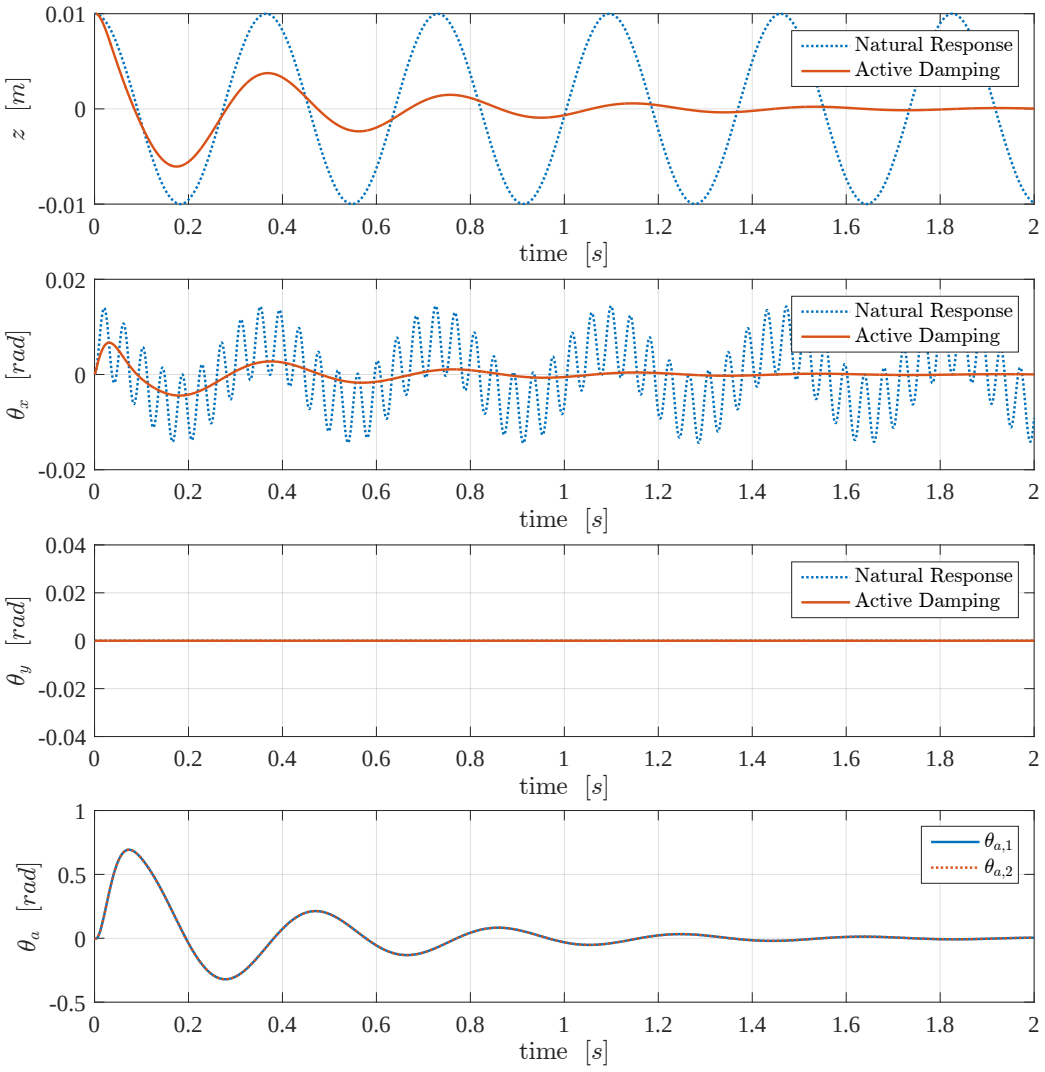

Figure 3.4: Simulated response of the linearised models for test case 1

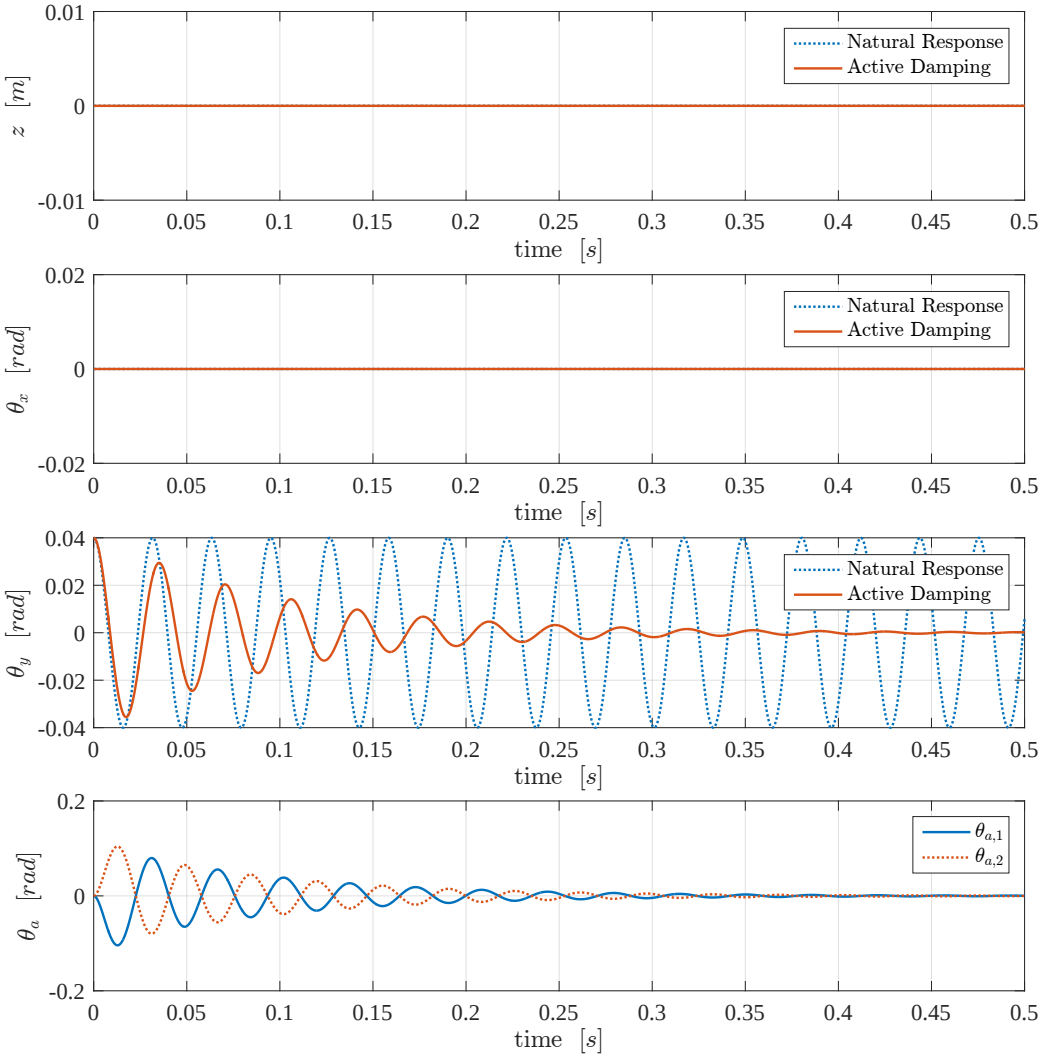

Figure 3.5: Simulated response of the linearised models for test case 2

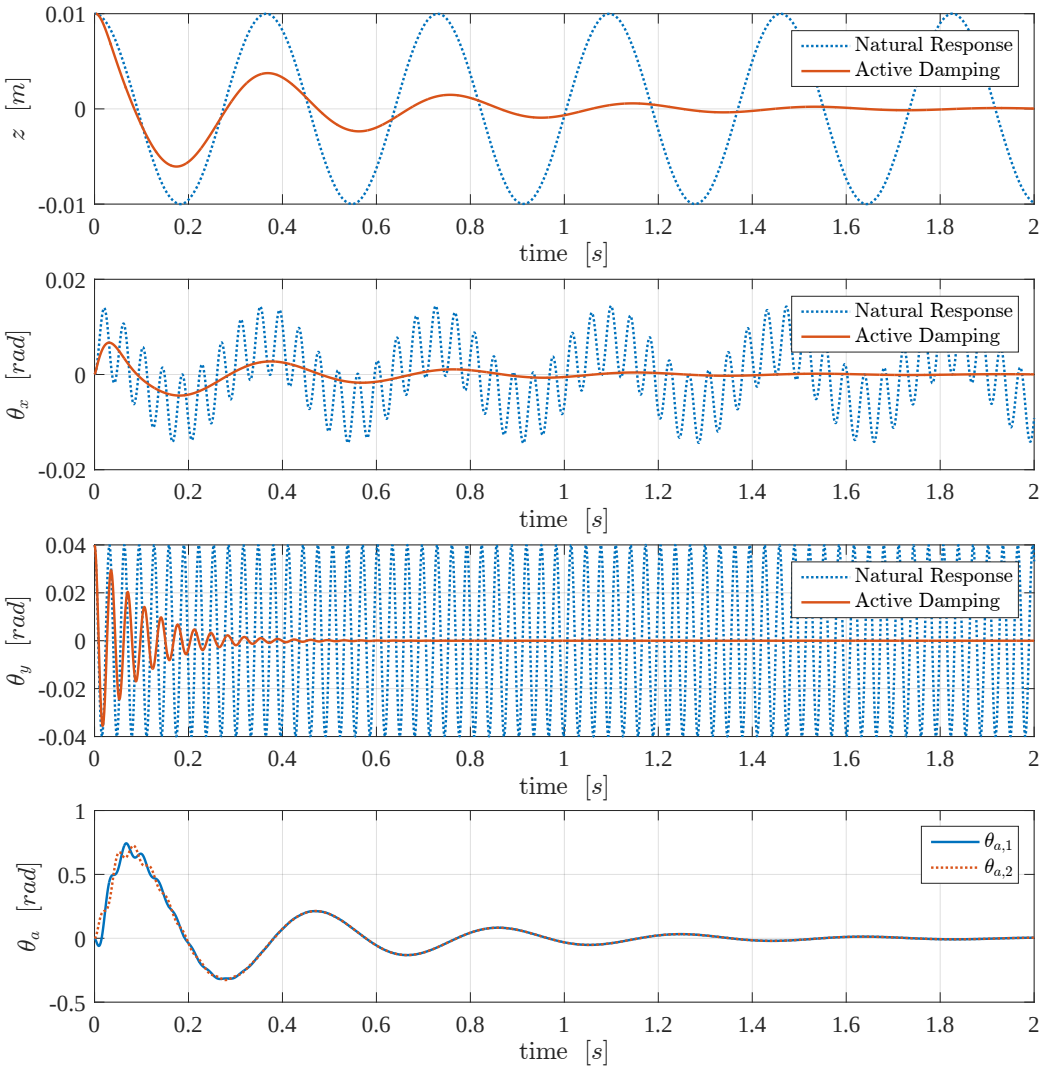

Figure 3.6: Simulated response of the linearised models for test case 3

Chapter 4

Multi-Axis Vibration Controller Design

For the purposes of controller design, the mobile platform dynamics can be divided into two independent subsystems corresponding to the in-plane and out of plane dynamics. Each subsystem contains three degrees of freedom. Such a design procedure can be performed because of the fact there is no dynamic coupling between the two subsystems. Additionally the out of plane modes are completely uncontrollable via cable actuation.

In this chapter, control methods are developed for persistent excitations of the platform which may occur along any of the platform's six spatial degrees of freedom. Section 4.1 investigates vibration control of the in-plane dynamics via cable actuation. Section 4.2 develops a control strategy for the multi-axis reaction system (MARS) introduced in Chapter 3.

In Section 4.3, observers and state estimation procedures using available sensor data are developed and presented.

In the final section of this chapter, the effectiveness of the controllers developed in Sections 4.1 and 4.2 is demonstrated in simulation.

4.1 In-Plane Control

A high level block diagram outlining the overall control topology for the in-plane system can be found in Figure 4.1. In the proceeding subsections, the elements of Figure 4.1 will be developed and described in detail.

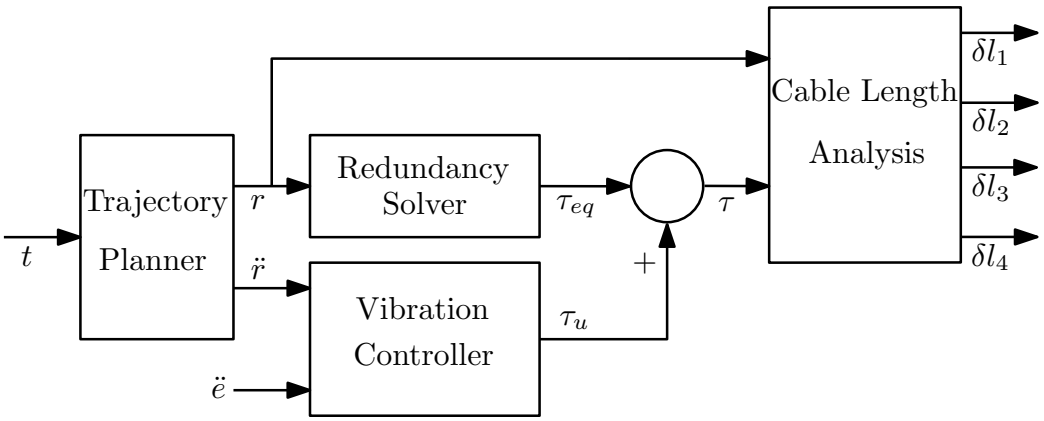

Figure 4.1: High level in-plane control architecture

4.1.1 Trajectory Planner

From a motion planning perspective, a planar manipulator is simply a three degree of freedom system. Because of the geometric constraints imposed by the redundant cables, the rotation of the mobile platform about the planar normal axis can be assumed fixed. This reduces the functional workspace further to consist of merely two degrees of freedom: translation about the planar horizontal and vertical axes. For the intended application of pick and place operations in a warehouse, trajectory planning is fairly simple. There are no obstacles to avoid and motion tasks generally consist of moving to a location, stopping to pick up and object, moving to a second location, and stopping to drop the object. To serve this purpose a simple waypoint tracking controller was developed.

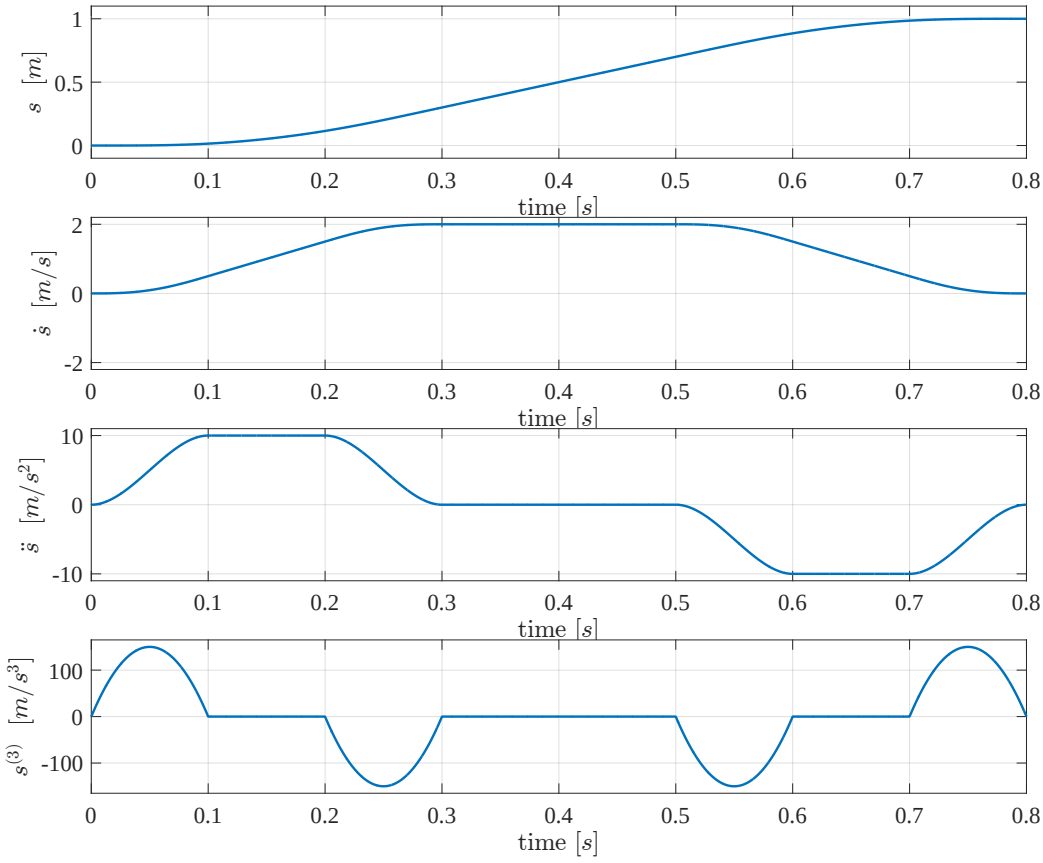

Figure 4.2: Kinematic profile with cubic accelerations

The task of the waypoint tracking controller is as follows: given an ordered set of n points, the platform must move from a given starting position and pass through each point sequentially. In this particular implementation, the platform must stop at each waypoint before proceeding to the next. Consider w_i, the ith waypoint, where $i = 1 \cdots n-1$. A vector pointing from the current waypoint to the next can be obtained as:

$$v = w_{i+1} - w_i \tag{4.1}$$

The unit vector pointing toward the next waypoint from the current is

then simply $\hat{v} = \frac{v}{\|v\|}$. A trajectory from the current to the next waypoint can then be defined as:

$$v_r = w_i + s \cdot \hat{v} \tag{4.2}$$

where s is a time varying parameter such that $0 \leq s \leq \|v\|$. At the beginning of the tracking sequence, $i = 1$ and w_1 is the initial position of the platform. The platform then follows the trajectory defined by (4.2). Upon reaching the next waypoint, the value of i is iterated. This process continues until $i = n$, at which point, the motion sequence is complete.

The time varying parameter s was designed to produce a cubic acceleration profile. The benefit is such a kinematic profile is that the acceleration and jerk are continuous. This is helpful for minising shocks and vibrations in the system. Figure 4.2 shows an example of the form of kinematic profiles used for designing the trajectory parameter s. For a detailed explanation of how a cubic acceleration motion profile can be derived, the reader is refered to [35].

4.1.2 Cable Length Analysis

If the position and orientation of the platform is known, the cable lengths can be determined via the cable model of Section 3.1.2, specifically, (3.7). If it is desired to produce a particular tension within a cable, the required cable unstretched length to produce such a tension can be found by solving (3.8) for δl_i.

4.1.3 Redundancy Solver

The redundancy solver is based on a slightly modified version of the warehousing robot dynamic model presented in Chapter 3. Since the twelve cables of the robot are driven by only four actuators, it is beneficial for the sake of clarity to restate the twelve cable system as an equivalent four cable system.

The mounting points for the twelve cables are designed such that the length of all cables in a single control group are the same. Exploiting this knowledge, each of the four cable control groups can be collapsed to a single equivalent cable. Effective cables 1, 2, 3, and 4 correspond to the cable groups driven by the top-left, top-right, bottom-left, and bottom-right motors respectively. F_x, F_y, and M_z, the combined forces and moment applied on the mobile platform by the cables, are found to be:

$$\begin{aligned} F_x &= \sum_{i=1}^{4} \left(\tau_i \hat{c_i} \cdot \hat{i} \right) \\ F_y &= \sum_{i=1}^{4} \left(\tau_i \hat{c_i} \cdot \hat{j} \right) \\ M_z &= \sum_{i=1}^{4} \left((r_{c,i} \times \tau_i \hat{c_i}) \cdot \hat{k} \right) \end{aligned} \tag{4.3}$$

where τ_i is the tension of the ith equivalent cable. The coefficients of (4.3) in terms of τ_{1-4} can be collected into a matrix, A, defined as:

$$A = \begin{bmatrix} \hat{c}_1 \cdot \hat{i} & \hat{c}_2 \cdot \hat{i} & \hat{c}_3 \cdot \hat{i} & \hat{c}_4 \cdot \hat{i} \\ \hat{c}_1 \cdot \hat{j} & \hat{c}_2 \cdot \hat{j} & \hat{c}_3 \cdot \hat{j} & \hat{c}_4 \cdot \hat{j} \\ (r_{c,1} \times \hat{c}_1) \cdot \hat{k} & (r_{c,2} \times \hat{c}_2) \cdot \hat{k} & (r_{c,3} \times \hat{c}_3) \cdot \hat{k} & (r_{c,4} \times \hat{c}_4) \cdot \hat{k} \end{bmatrix} \tag{4.4}$$

Using the matrix A defined above, the following linear relationship relating cable tensions to the forces applied on the box can be obtained:

$$A\,\tau = u \tag{4.5}$$

where $\tau = \begin{bmatrix} \tau_1 & \tau_2 & \tau_3 & \tau_4 \end{bmatrix}^T$ and $u = \begin{bmatrix} Fx & Fy & Mz \end{bmatrix}^T$. Since the system is redundantly actuated, there are an infinite number of solutions for τ to produce a desired u. In order to solve the redundancy issue, some sort of optimisation

procedure is required in order to select a particular solution which is most desirable. Perhaps the simplest approach is to set the cable tensions to their maximum permissible values. The justification for using such an approach is supported by the work of Behzadipour and Khajepour who, in [16], proved that the stiffness of a cable driven manipulator can always be improved by increasing the internal forces.

Maximum tension limits τ_{tm} and τ_{bm} are imposed on the tensions of the top and bottom cables respectively. Expressed as a set of inequalities:

$$\begin{aligned} \tau_1, \tau_2 &\leq \tau_{tm} \\ \tau_3, \tau_4 &\leq \tau_{bm} \end{aligned} \tag{4.6}$$

By restricting one of cable tensions to its maximum value, A can be reduced to a 3x3 matrix, at which point the system is no longer redundantly constrained and a solution for the remaining tensions can be found by solving (4.5) for τ. Define $\tau_{m,i}$ as the set of tensions obtained by restricting the tension of cable i to its maximum value, then for all $j \neq i$, if $\|\tau_{m,i}\| > \|\tau_{m,j}\|$, $\tau_{opt} = \tau_{m,i}$.

At static equilibrium, $u = u_{eq} = \begin{bmatrix} 0 & m_p g & 0 \end{bmatrix}^T$. Therefore, the optimal set of cable tensions required to maintain a state of static equilibrium for the mobile platform, τ_{eq}, is equivalent to τ_{opt} when $u = u_{eq}$.

4.1.4 Decoupled PD Control

By linearising the platform dynamics about a static equilibrium point, the following simplified model of the planar dynamics resulting from cable elongation can be obtained:

$$\begin{aligned} \ddot{x} &= -k_x x + F_x \\ \ddot{y} &= -k_y y + F_y \\ \ddot{\phi} &= -k_\phi \phi + M_z \end{aligned} \tag{4.7}$$

where $k_x, k_y,$ and k_ϕ are equivalent stiffnesses resulting from the combined stiffnesses of the individual cables. The three control inputs, $F_x, F_y,$ and M_z, represent the forces which can be applied by varying the unstretched cable lengths from their equilibrium lengths. The problem then becomes how to chose $F_x, F_y,$ and M_z in order to adequately keep the platform along its equilibrium trajectory and eliminate task space position errors caused by cable elongation. One potential candidate is to use three independent PD controllers, constraining the three inputs to the following form:

$$u = \begin{bmatrix} F_x \\ F_y \\ M_z \end{bmatrix} = \begin{bmatrix} K_{p,x}\, \hat{e}_x + K_{d,x}\, \hat{\dot{e}}_x \\ K_{p,y}\, \hat{e}_y + K_{d,y}\, \hat{\dot{e}}_y \\ K_{p,\phi}\, \hat{e}_\phi + K_{d,\phi}\, \hat{\dot{e}}_\phi \end{bmatrix} \tag{4.8}$$

where $\hat{e}_x, \hat{e}_y,$ and $\hat{e}_\phi$ correspond to the estimates of the task space tracking errors, as defined in Section 4.3.1. The requested command forces of u can be converted to cable tensions using the following relationship:

$$\tau_u = A^+ u \tag{4.9}$$

where A^+ is the Moore–Penrose pseudoinverse of matrix A which is defined in (4.4). This results in a solution whose demand for the required change in cable tensions is a minimum, in terms of the Euclidean norm. Combining the control tensions with the static equilibrium tensions, which are determined as defined in Section 4.1.3, the total required cable tension commands can be obtained as:

$$\tau = \tau_{eq} + \tau_u \tag{4.10}$$

4.1.5 Input Saturation

It is necessary to limit how much the tension in each cable can be varied by any active vibration controller. Without such limitations, there is no guarantee that cable tensions will remain within a range that is both safe for operation and producible by the actuators.

Define τ_{max} as the maximum change in tension that can be applied to a single cable by the vibration controller. τ_u is a vector which contains the requested change in tensions for the i cables and is defined as $\tau_u = \begin{bmatrix}\tau_{u,1} \ \tau_{u,2} \ \tau_{u,3} \ \tau_{u,4}\end{bmatrix}^T$. If the components of τ_u are to be considered valid, for $i = 1 \ldots 4$, the following inequality must hold:

$$\|\tau_{u,i}\| \leq \tau_{max} \tag{4.11}$$

Consider u_d as the unsaturated applied force request vector, generated by the active vibration controller. From Section 4.1.3, the cable tensions required to produce a given u can be found by solving $\tau_u = A^+ u$. Simply saturating the individual components of τ_u is inadequate as the forces applied to the mobile platform are not the tensions of individual cables but a combination thereof. As a result, if tensions are saturated individually, the resulting applied forces become skewed and no longer a proper representative of u_d. Consider, provided that $\hat{u}_d = u_d / \|u_d\|$, u_d can be restated as:

$$u_d = \|u_d\| \cdot \hat{u}_d \tag{4.12}$$

In order for the directional integrity of u_d to be maintained after saturation, u must be expressible as $\alpha \cdot \hat{u}_d$, where α is some real scalar. With this in mind, (4.9) can be restated as:

$$\tau_u = \left(A^{+}\hat{u}_d\right) u_{sat} \tag{4.13}$$

where $u_{sat} \leq \|u_d\|$ is the largest possible positive scalar such that (4.11) is satisfied. (4.13) can be simplified as:

$$\begin{bmatrix} \tau_1 \\ \tau_2 \\ \tau_3 \\ \tau_4 \end{bmatrix} = \begin{bmatrix} a_1 \\ a_2 \\ a_3 \\ a_4 \end{bmatrix} u_{sat} \tag{4.14}$$

The maximum possible value for u_{sat} then can be found as:

$$u_{sat} = \min \left\{ \|u_d\|, \left|\frac{\tau_{max}}{a_1}\right|, \left|\frac{\tau_{max}}{a_2}\right|, \left|\frac{\tau_{max}}{a_3}\right|, \left|\frac{\tau_{max}}{a_4}\right| \right\} \tag{4.15}$$

4.2 MARS Controller Design

It is important to consider the nonlinear dynamics of the pendulums when designing a controller for the multi-axis reaction system (MARS) introduced in Chapter 3. Close to the stable equilibrium point, when the pendulums are aligned with the gravity vector, a linearised approximation of the dynamics could be used and a controller designed using any of the many various linear control design methods. However, when the amplitudes of the out of plane oscillations become large, the angular positions of the pendulums as they try to compensate the large position errors will become similarly large and venture away from the region in which the local linear approximation is valid. This poses a concern not only for potential degradation in performance, but also for the stability of the system.

Another important consideration is the robustness features for the chosen controller. Given that the intended application of the CDPR under consideration is performing pick and place operations within a warehousing environment, it is important that the MARS controller remains stable and

effective in the presence of large variations in the platform mass. It is also important that the controller can tolerate the changes in the out of plane dynamics which result from varying the position of the platform within the plane.

For the reasons mentioned above, a sliding mode control approach has been pursued because of its excellent robustness features and ability to handle the nonlinear pendulum dynamics. Since the subsystem governing the out of plane and pendulum dynamics is underactuated, a hierarchical sliding surface design is used.

This type of controller is based off of the work presented in [36] and [37]. The basic concepts and specific controller design relevant to this system are presented in the proceeding subsections.

4.2.1 Hierarchical Sliding Surface Design

The out of plane dynamics of the mobile platform with a single pendulum actuator can be divided into a set of subsystems corresponding to the dynamics of z, θ_x, θ_y, and θ_p. These four subsystems are driven by a single input: the torque applied by the motor coupled to the pendulum. The dynamic equations of the system, derived in Chapter 3, can be arranged to fit the following form:

$$\begin{aligned} \ddot{z} &= f_1 + b_1 u + d_1 \\ \ddot{\theta}_x &= f_2 + b_2 u + d_2 \\ \ddot{\theta}_a &= f_3 + b_3 u + d_3 \end{aligned} \tag{4.16}$$

f_i, and b_i are nonlinear functions of X and time where X is the complete state vector. The d_i terms represent lumped disturbances which account for the effects of modeling errors, external disturbances, and unmodeled dynamics (such as the coupled dynamics between θ_y and θ_a).

Define a set of i sliding surfaces of (4.16), corresponding to the i subsystems, where $i = 1 \dots 3$, as:

$$\begin{aligned} s_1 &= c_1 z + \dot{z} \\ s_2 &= c_2 \theta_x + \dot{\theta}_x \\ s_3 &= c_3 \theta_a + \dot{\theta}_a \end{aligned} \tag{4.17}$$

where c_i is a constant, chosen such that s_i is stable. After taking the derivative of surface s_i, with the knowledge that in the sliding phase, $s_i = \dot{s}_i = 0$, the equivalent control required to keep the ith subsystem along its sliding surface can be found as:

$$u_{eq,i} = -\frac{f_i + c_i x_j}{b_i} \tag{4.18}$$

A hierarchical sliding surface, S, can then be formed using a linear combination of the subsystem surfaces, scaled using a set of i parameters.

$$S = \alpha_1 s_1 + \alpha_2 s_2 + \alpha_3 s_3 \tag{4.19}$$

Now that a sliding surface has been designed, the control input, u, required to force the system to the sliding state in finite time can be found using stability analysis.

4.2.2 Control Design

Consider the following candidate Lyapunov function:

$$V = \frac{1}{2} S^2 \tag{4.20}$$

Taking the time derivative of (4.20) and making some necessary substitutions and algebraic manipulations we can end up with the following expression:

$$
\begin{aligned}
\dot{V} &= S\dot{S} \\
&= S\left[\alpha_1 \dot{s_1} + \alpha_2 \dot{s_2} + \alpha_3 \dot{s_3}\right] \\
&= S\left[\alpha_1 \left(c_1 \dot{z} + \ddot{z}\right) + \alpha_2 \left(c_2 \dot{\theta}_x + \ddot{\theta}_x\right) + \alpha_3 \left(c_2 \dot{\theta}_p + \ddot{\theta}_p\right)\right] \\
&= S\left[\alpha_1 \left(c_1 \dot{z} + f_1 + b_1 u\right) + \alpha_2 \left(c_2 \dot{\theta}_x + f_2 + b_2 u\right) + \alpha_3 \left(c_2 \dot{\theta}_p + f_3 + b_3 u\right)\right] \\
&= S\left[\left(\alpha_1 b_1 + \alpha_2 b_2 + \alpha_3 b_3\right) u - \left(\alpha_1 b_1 \, u_{eq,1} + \alpha_2 b_2 \, u_{eq,2} + \alpha_3 b_3 \, u_{eq,3}\right)\right]
\end{aligned}
\tag{4.21}
$$

Assume that the value of $\dot{S}$ is as follows:

$$
\dot{S} = -\eta \, \mathrm{sign}(S) - kS \tag{4.22}
$$

where η and k are positive constants. By rearranging the expression for $\dot{S}$ contained in the last line of (4.21), the switching control signal, u_{sw}, can be obtained as:

$$
u_{sw} = \frac{\left(\alpha_1 b_1 \, u_{eq,1} + \alpha_2 b_2 \, u_{eq,2} + \alpha_3 b_3 \, u_{eq,3}\right) - \eta \, \mathrm{sign}(S) - kS}{\left(\alpha_1 b_1 + \alpha_2 b_2 + \alpha_3 b_3\right)} \tag{4.23}
$$

Substituting (4.23) for the u term of (4.21), the expression for $\dot{V}$ reduces to:

$$
\dot{V} = -\eta |S| - kS^2 \tag{4.24}
$$

Which is negative definite, therefore satisfying the Lyapunov condition for asymptotic stability. Thus, it has been proven that with the application of the switching control signal, u_{sw}, the system dynamics will converge asymptotically to the Hierarchical sliding surface of (4.19). Reformulating (4.21) to include the disturbance terms present in (4.16) and using the same switching control of (4.23):

$$\begin{aligned}\dot{V} &= S\left[-\eta\,\mathrm{sign}(S) - kS + (\alpha_1 d_1 + \alpha_2 d_2 + \alpha_3 d_3)\right] \\ &= -\eta|S| - kS^2 + S\left(\alpha_1 d_1 + \alpha_2 d_2 + \alpha_3 d_3\right) \\ &\leq -\eta|S| - kS^2 + |S|\,|\alpha_1 d_1 + \alpha_2 d_2 + \alpha_3 d_3|\end{aligned} \tag{4.25}$$

Therefore, given a sufficiently large switching gain, η, such that $\eta \geq |\alpha_1 d_1 + \alpha_2 d_2 + \alpha_3 d_3|$, the sliding surface dynamics are invariant to the combined lumped disturbances.

4.3 Vibration Observer and State Estimation

Using the inverse kinematic model described in Section 4.1.2, the set of unstretched cable lengths required to bring the mobile platform to a particular desired location can be determined. The required lengths can then be fed into the cable reel motor's controllers and the mobile platform's new equilibrium position will be brought to the desired location. This is the functioning procedure of a joint space controller.

Joint space control works well if the links connected to said joints do not experience a significant degree of deformation. If deformation does occur, such as in the form of bending, or more specifically in this case, elongation, then the effectiveness of joint space control breaks down.

When cable elongation occurs between the cable spool and platform, the resulting change in length of the cables is imperceptible with only knowledge of the spool position. The effect of this is that any deviations in the position of the platform resulting from cable elongations requires additional knowledge in order to be observable. The proceeding subsections describe how this problem has been addressed and incorporated within the overall controller design.

4.3.1 IMU Integration

Mounted aboard the mobile platform is a 6-axis Inertial Measurement Unit (IMU). The IMU produces three acceleration measurements $(\ddot{x}, \ddot{y}, \ddot{z})$ and three angular velocity measurements $(\omega_x, \omega_y, \omega_z)$.

From the trajectory planner, the desired accelerations $(\ddot{x}_d, \ddot{y}_d)$ in the x and y directions are known. Subtracting the measured accelerations from the desired accelerations, an estimation of the second rates of the tracking errors can be obtained. Namely:

$$\begin{aligned} \ddot{e}_x &= \ddot{x}_d - \ddot{x}_m \\ \ddot{e}_y &= \ddot{y}_d - \ddot{y}_m \\ \ddot{e}_z &= -\ddot{z}_m \end{aligned} \tag{4.26}$$

where $\ddot{x}_m$ and $\ddot{y}_m$ are the measured x and y accelerations respectively. By integrating $\ddot{e}$, an estimate of $\dot{e}$ can be found and further integration produces and estimate of e. However, due to the fact that IMU measurements are not perfect and often contain considerable noise and constant bias, simply integrating $\ddot{e}$ leads to a rapid deterioration of the estimates for $\dot{e}$ and e as they start to drift away from the result of accumulated errors.

It is known, due to the imposition of tracking error limits on the cable lengths, that the tracking errors on the unstretched cable lengths are very small. Because of this, it can be assumed that any measured tracking error estimates obtained from the IMU are a result of effects such as cable elongation which cannot be directly observed from the measured unstretched lengths. Based on this assumption, an additional set of assumptions can be made: for a large enough window, the moving averages of $\ddot{e}$, $\dot{e}$, and e are zero. Based on these assumptions, the estimates $\hat{e}$ of e can be improved be subtracting the computed moving averages from the measured estimates of $\ddot{e}$, $\dot{e}$, and e. This helps to remove the effects of accumulated noise and constant

biases and prevents the computed estimates from diverging. The length of a well performing window size for the moving averages are sensor dependent and can be tuned experimentally until a satisfying result is obtained. A block diagram representation of the complete IMU integration filter is provided in Figure 4.3.

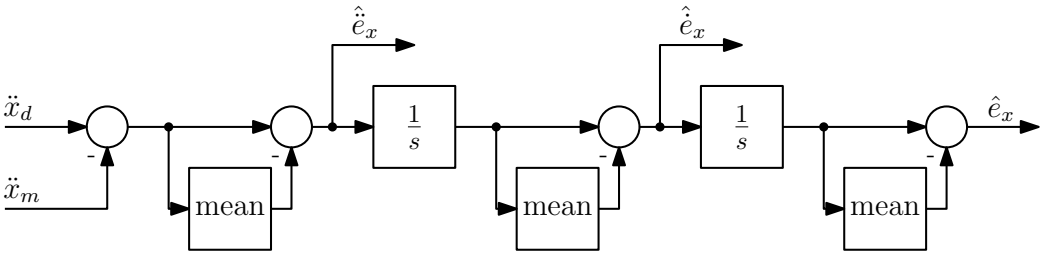

Figure 4.3: IMU based filter for obtaining estimates of tracking errors

A similar approach can be taken for obtaining estimates of e_z, e_ψ, e_θ and e_ϕ. Since the gyroscopes measure angular velocity rather than angular acceleration, a slight modification is necessary as the first set of integrations are no longer necessary, $\dot{e}$ can be computed directly as:

$$\begin{aligned} \dot{e}_\psi &= -\omega_x, \\ \dot{e}_\theta &= -\omega_y, \\ \dot{e}_\phi &= -\omega_z \end{aligned} \tag{4.27}$$

4.3.2 Sliding Mode Differentiator

The angular position of the pendulums are directly measurable using encoders coupled to the motor shafts. The angular velocities however are not available and so, some form of numerical differentiation is required. Numerical differentiation of real life signals is notoriously difficult. The effects of noise and discretization errors are greatly amplified through the act of differentiation. In order to obtain estimates for the pendulum angular velocities,

a 2nd order sliding mode exact robust differentiator was used. This type of filter, originally presented in [38, 39], has been observed to perform very well in terms of noise rejection and induced signal lag. It's implementation is simple and it is computationally inexpensive. The applied filter is presented below:

$$\begin{aligned}
\dot{z}_0 &= -\lambda_2 L^{1/3} \left| z_0 - \theta_a \right|^{2/3} \operatorname{sign}(z_0 - \theta_a) + z_1 \\
\dot{z}_1 &= -\lambda_1 L^{1/2} \left| z_1 - z_0 \right|^{1/2} \operatorname{sign}(z_1 - z_0) + z_2 \\
\dot{z}_2 &= -\lambda_0 L \operatorname{sign}(z_2 - z_1)
\end{aligned} \tag{4.28}$$

For the measured signal, θ_a, with proper parameter selection, it can be shown that in finite time, and in the absence of noise, $z_0 = \theta_a,$ and $z_1 = \dot{\theta}_a$. In the filter presented above, $\lambda_0, \lambda_1, \lambda_2,$ and L are design parameters which can be used to tune the performance of the filter. On suggestion from [39], the following λ values were chosen: $\lambda_0 = 1.1, \lambda_1 = 1.5, \lambda_2 = 3$. These values were found to work well. L was tuned experimentally using data measured from the pendulum encoders.

4.4 Simulated Controller Performance

In order to generate a realistic assessment for the performance of the controllers of Section 4.1 and 4.2, it is important to consider the nonlinear dynamics of both the warehousing robot and the pendulum actuators. To do so, a multi-body dynamic model of the warehousing robot system was developed using MapleSim.

Since no cable model exists within the standard MapleSim block set, instead the cables were modelled as a prismatic joint with a force that can be applied along the joint axis. The magnitude of the applied force was generated to replicate the behaviors of the single cable model presented in Section 3.1.2. Each cable was mounted to the fixed frame and the mobile

platform via spherical joints. Once the MapleSim had been developed, it was then exported to Simulink where controller design and simulation tasks were performed.

The results and a discussion of the insights gained from the simulation study of the active vibration controllers of Sections 4.1 and 4.2 are summarised and presented in Subsections 4.4.1 and 4.4.2 respectivly.

4.4.1 In-Plane Controller

For testing the decoupled PD control strategy, the platform was commanded to track a rectangular shaped trajectory. The same trajectory tracking task was repeated twice: once with no active vibration controller, and once with the decoupled PD controller enabled. Figure 4.4 shows the position tracking performance of the platform with and without active vibration control enabled. The controller signals generated by the decoupled PD controller during the motion are presented in Figure 4.5.

It can be observed that in the natural damping case (when the active vibration controller is disabled) the platform position in the y direction clearly contains a large oscillatory component. However, with the active vibration controller active, such persistent excitations are swiftly eliminated. In the x and θ_z directions, the amplitudes of the natural oscillatory motions are very small. This results from the fact that the stiffness of the cables used in this model is fairly high. Although vibrations in the x and θ_z directions are practically a non issue, it is still worth noting that the active damping controller does a good job at eliminating persistent excitations.

4.4.2 MARS Controller

Three different test cases are considered. In each test case, the mobile platform is given some initial condition and allowed to oscillate freely thereafter. In all of the results presented below, the active damping data sets correspond-

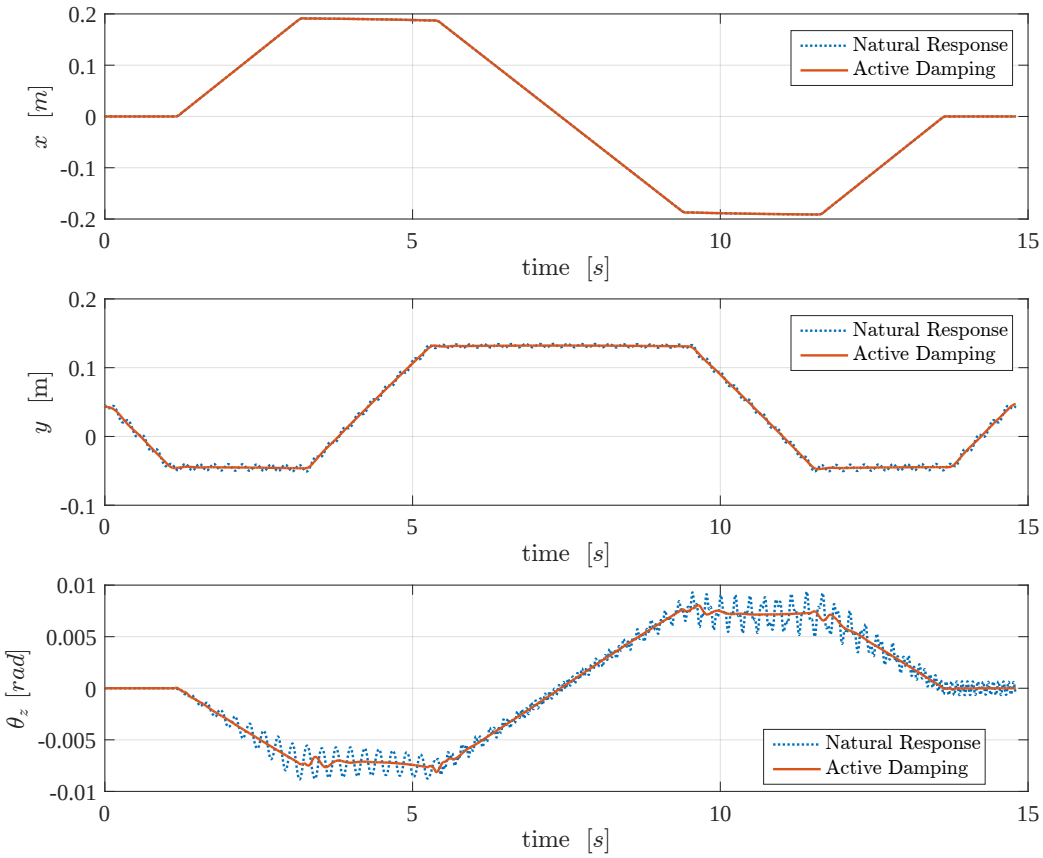

Figure 4.4: Simulated PD controller performance for rectangle trajectory

ing to the system response when the Hierarchical sliding mode controller is enabled. The natural damping data sets were obtained by observing the system response when the pendulums and platform are enabled to swing freely,(i.e. no actuator torque is applied along the motor shafts).

The simulated system response for test cases 1-3 are presented in Figures 4.6, 4.8, and 4.10 respectively. The control signals and the sliding surfaces of the hierarchical sliding mode controller are presented in Figures 4.7, 4.9, and 4.11 for test cases 1-3 respectively

In all three cases, the hierarchical sliding mode controller is observed to perform well and is a significant improvement over the natural damping case

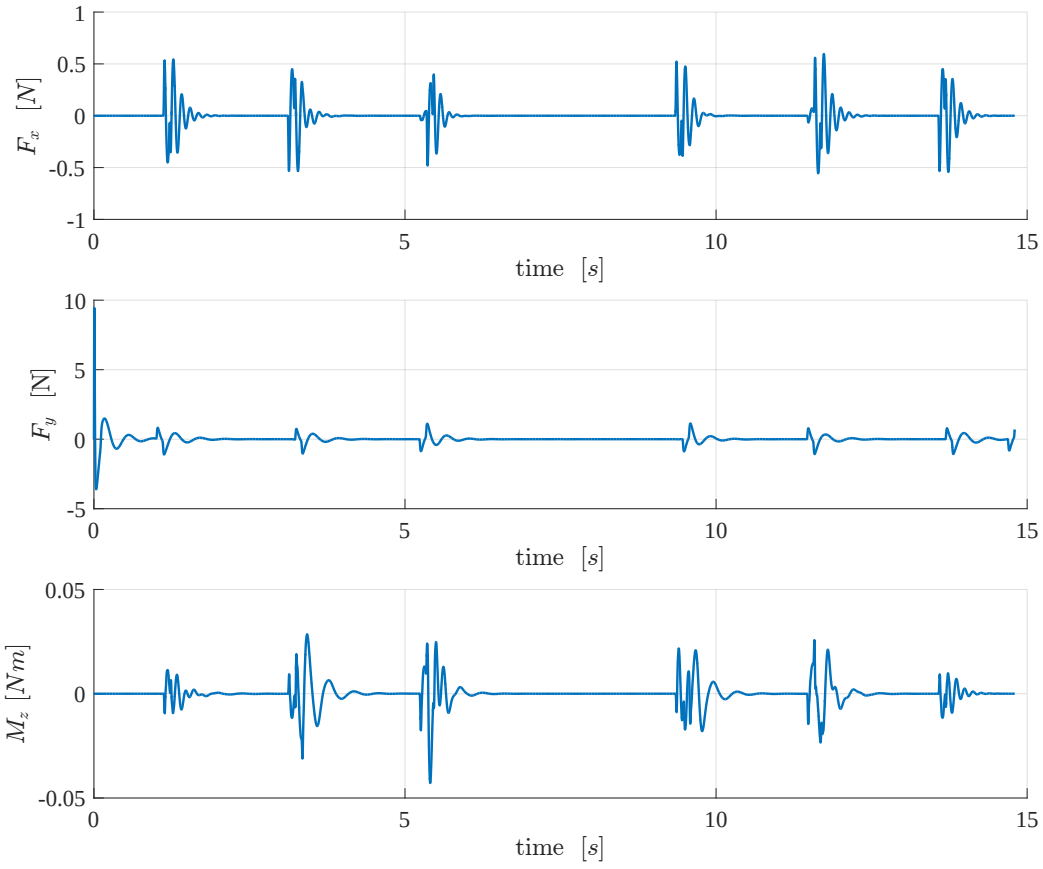

Figure 4.5: Simulated PD control signals for rectangle trajectory

of regulating any and all persistent excitations of the out of plane modes. Especially interesting is the result of test case 2, the results of which are presented in Figure 4.8. This test case clearly demonstrates that the hierarchical sliding mode controller is able to regulate persistent excitation of θ_y using only the disturbance rejection properties of the controller.

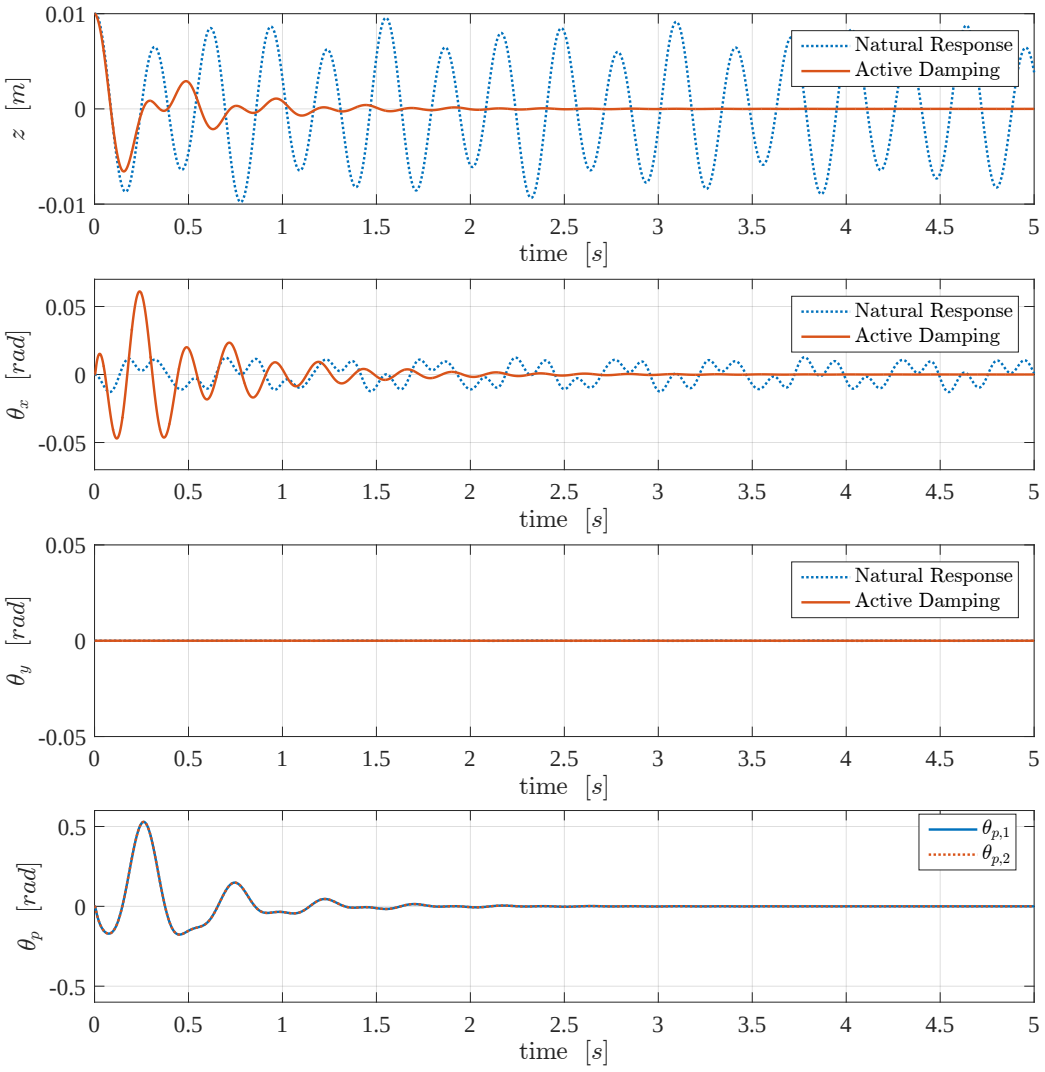

Figure 4.6: Simulated HSMC performance for case 1

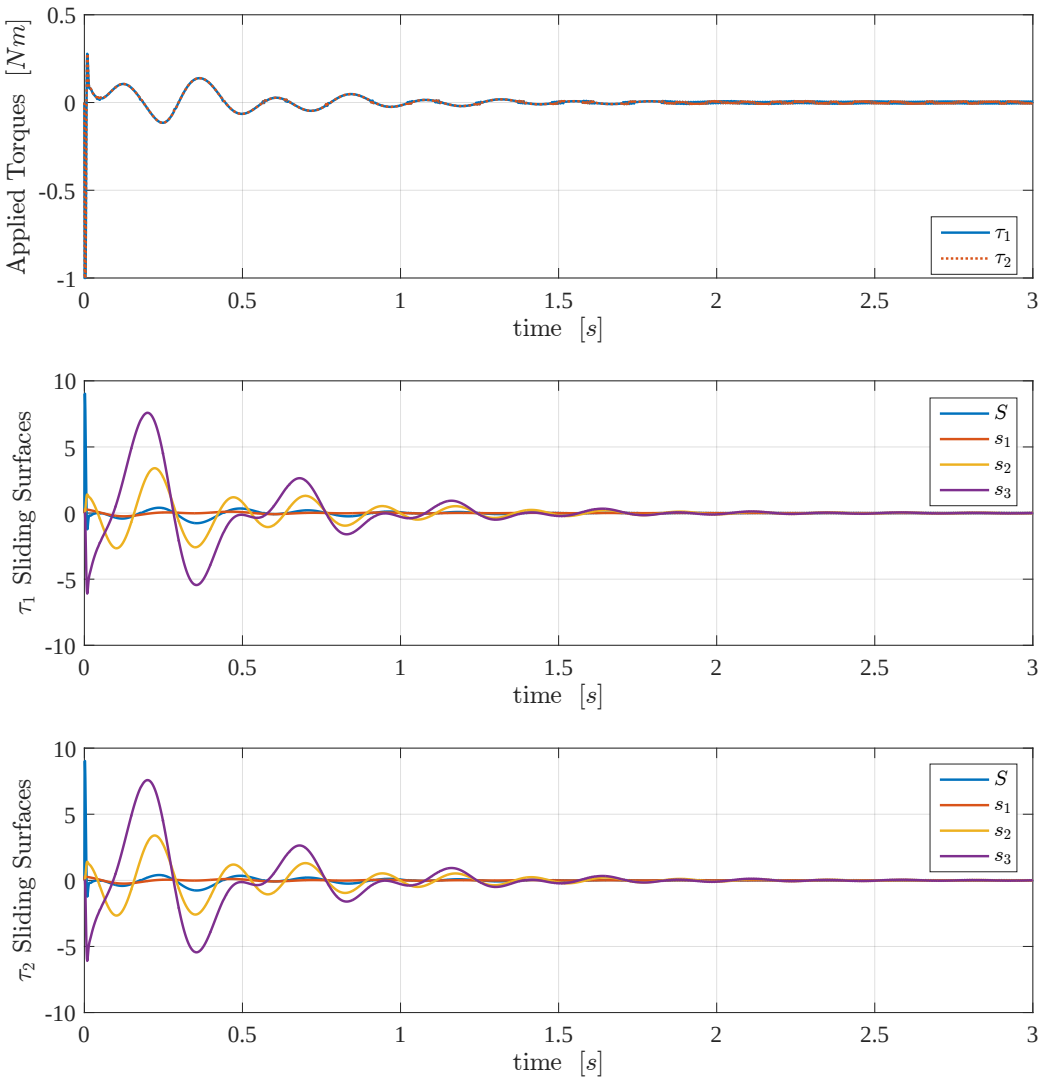

Figure 4.7: Simulated HSMC Control Signals for case 1

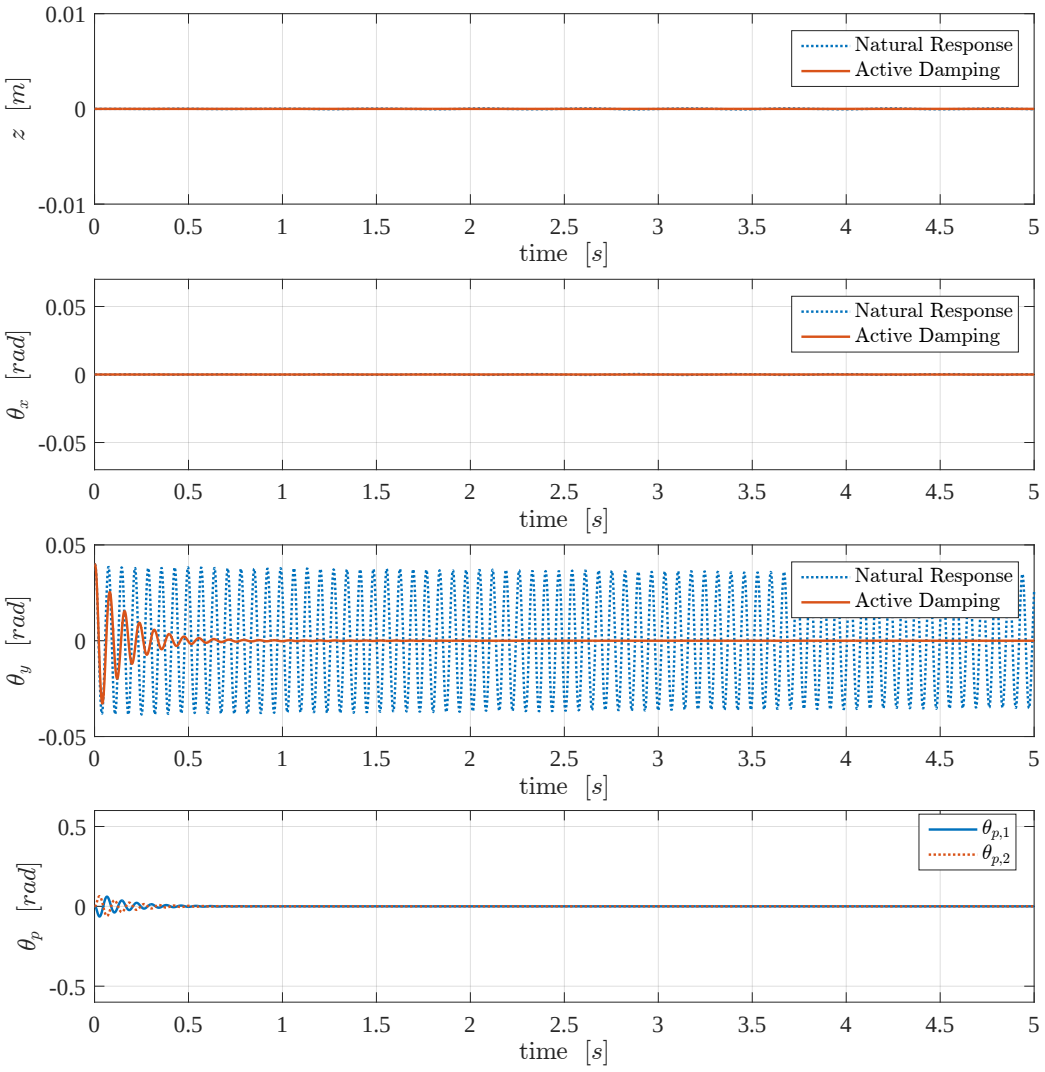

Figure 4.8: Simulated HSMC performance for case 2

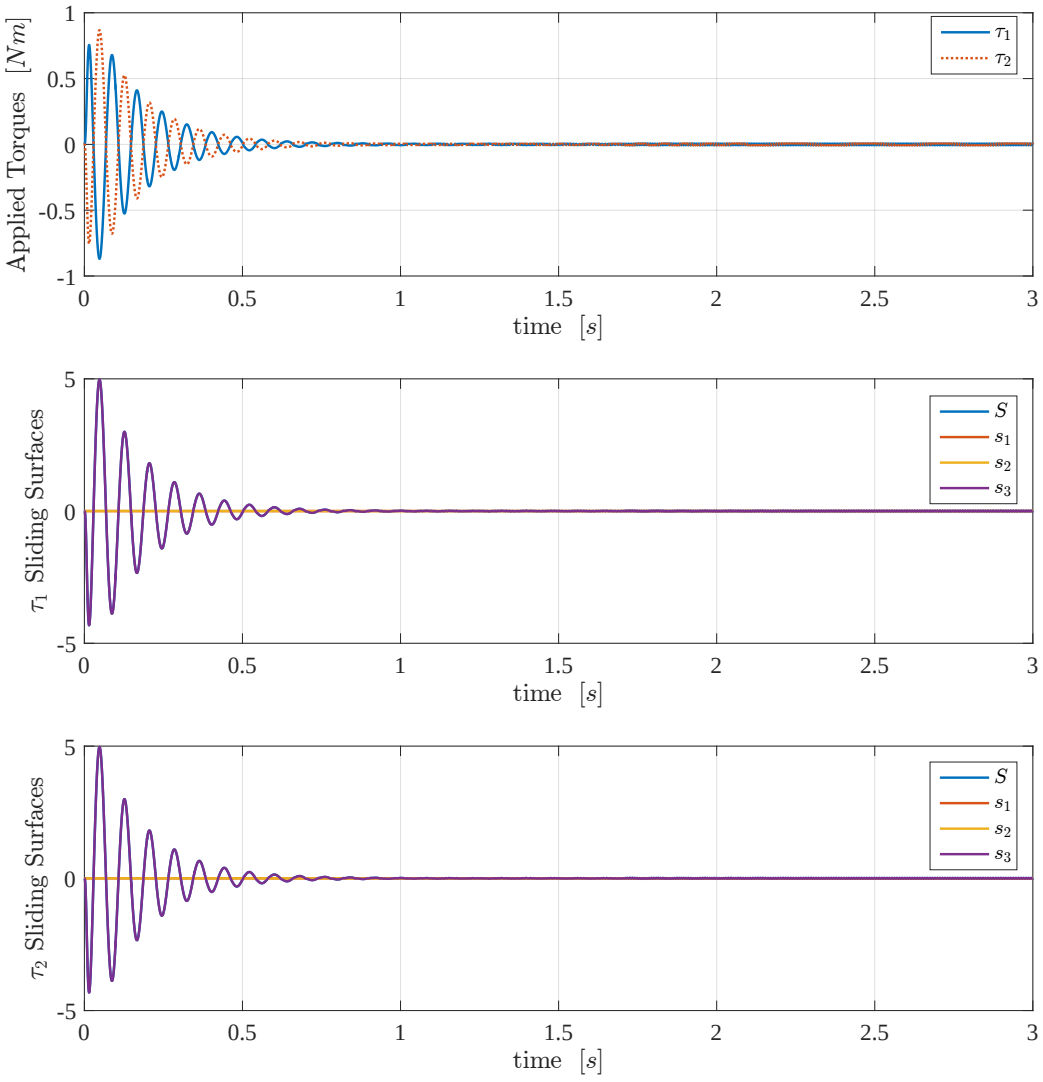

Figure 4.9: Simulated HSMC Control Signals for case 2

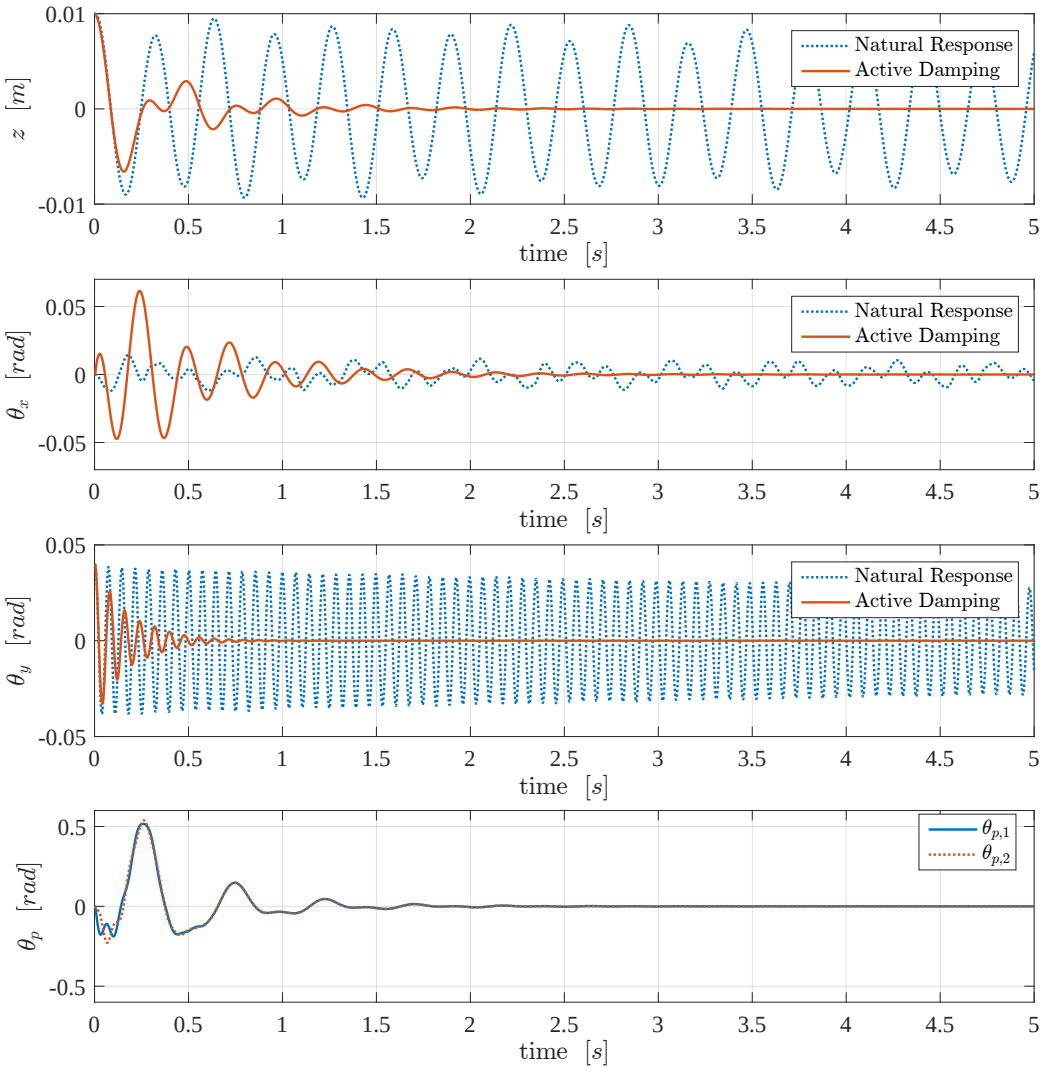

Figure 4.10: Simulated HSMC performance for case 3

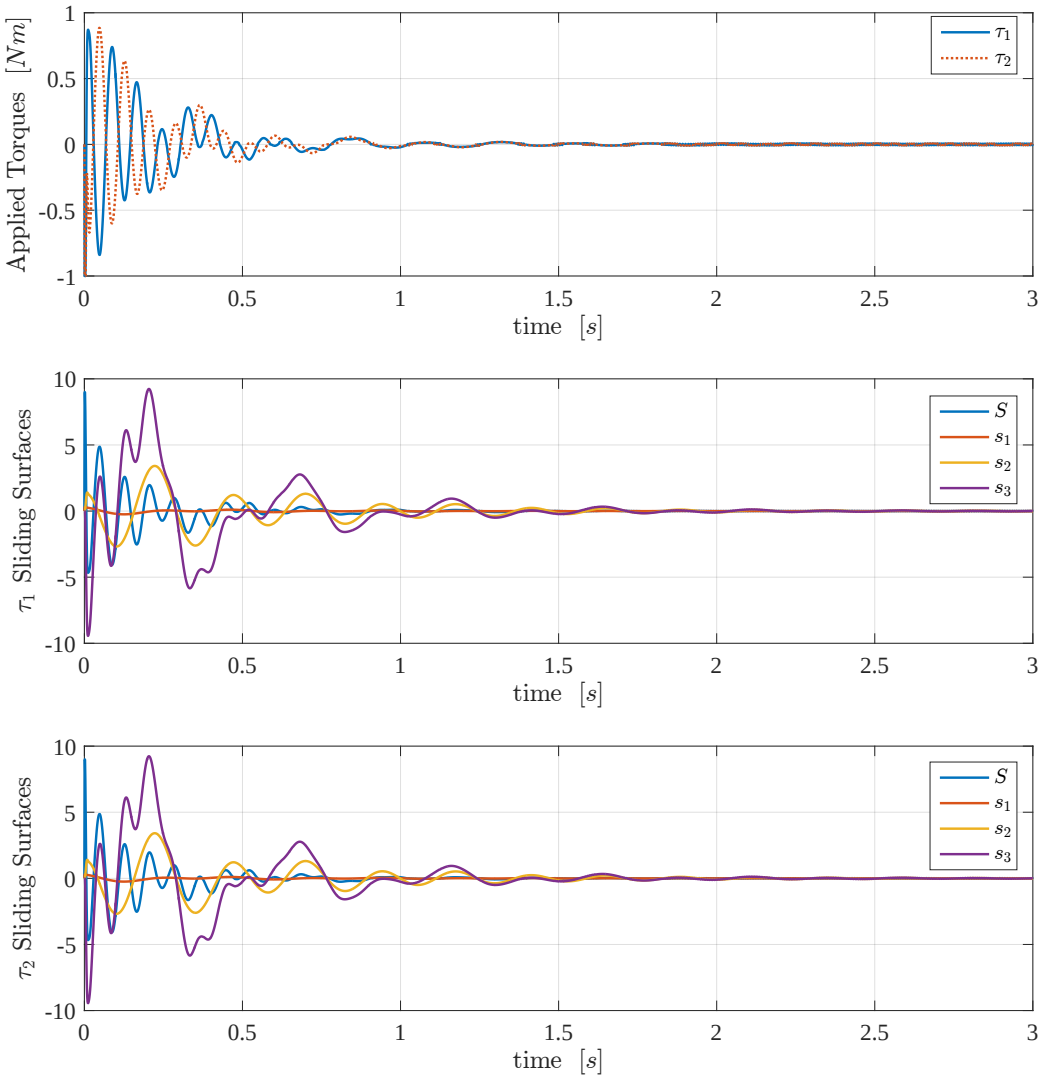

Figure 4.11: Simulated HSMC Control Signals for case 3

Chapter 5

Experimental Setup

The experimental test setup used for validating the work of Chapters 3 and 4 can be seen in Figure 5.1. It consists of three main elements: A cable driven parallel robot, intended for warehousing applications; a pair of pendulum actuators, designed and built based on the results of Chapter 3; and the software and realtime control hardware used for implementing and testing the control strategies of Chapter 4. In this chapter each of the three elements will be described in detail.

The chapter begins with Section 5.1 which provides a background and description of some of the mechanical properties for the cable-driven warehousing robot, inherited for this study.

Section 5.2 describes the realtime embedded control software design and overall architecture.

Section 5.3 provides details about the sensors used by the test setup for control and the necessary procedures that were taken to produce meaningful measurements.

Section 5.4 discuss a set of low level motor controllers which have been designed and implemented for directly controlling the unstretched cable lengths and cable tensions.

Section 5.5 is devoted presenting the design, construction, and integra-

tion of a pair of pendulum actuators into the preexisting warehousing robot system.

The procedures required for homing the warehousing robot and tensioning the cables are described in Section 5.6.

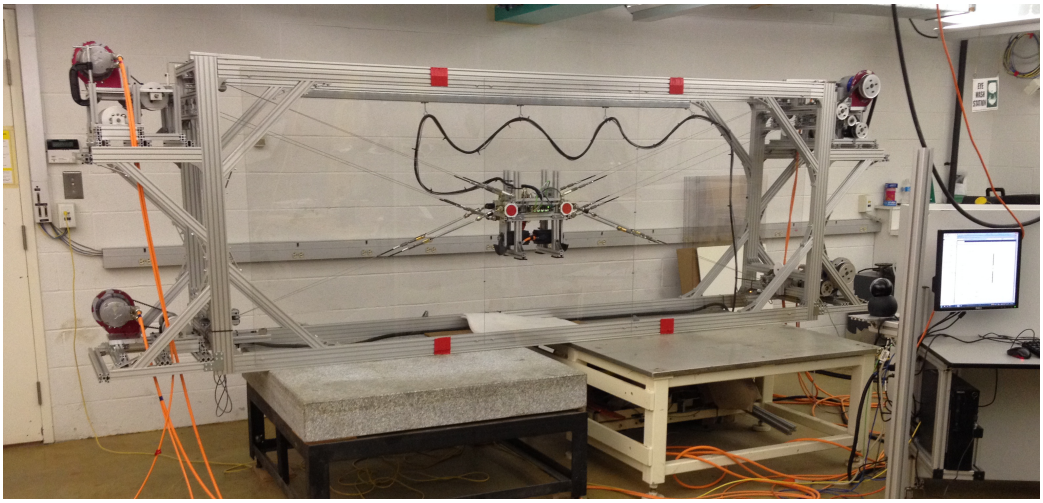

Figure 5.1: Experimental test setup

5.1 Warehousing Robot Prototype

The design for the CDPR was originally developed and presented by Mendez in [32] and is a scaled down version of a large scale CDPR intended for warehousing type applications. The mechanism consists of a rigid fixed frame and a rigid mobile platform which is suspended by twelve steel cables.

The length of the twelve cables are controlled by four Identical DC Motors attached to the fixed frame. The mechanism, despite having twelve cables, is effectively a four cable planar robot. Each of the four motors, which are placed in the four corners or the fixed frame, are responsible for actuating multiple cables simultaneously. The top motors each drive four cables and the bottom motors each drive two. The reason for the redundant cables is to

increase the manipulator stiffness, especially in the uncontrollable directions. A detailed discussion on the mechanical design and its merits can be found by referring to [32].

The cables are wound on spools which are coupled to the motors via a belt drive system. Figure 5.2 shows the power transmission system and cable spools for one of the lower motors. It can be seen that the belt drive system is also important for ensuring that the lengths of all the cable driven by a single motor are varied consistently.

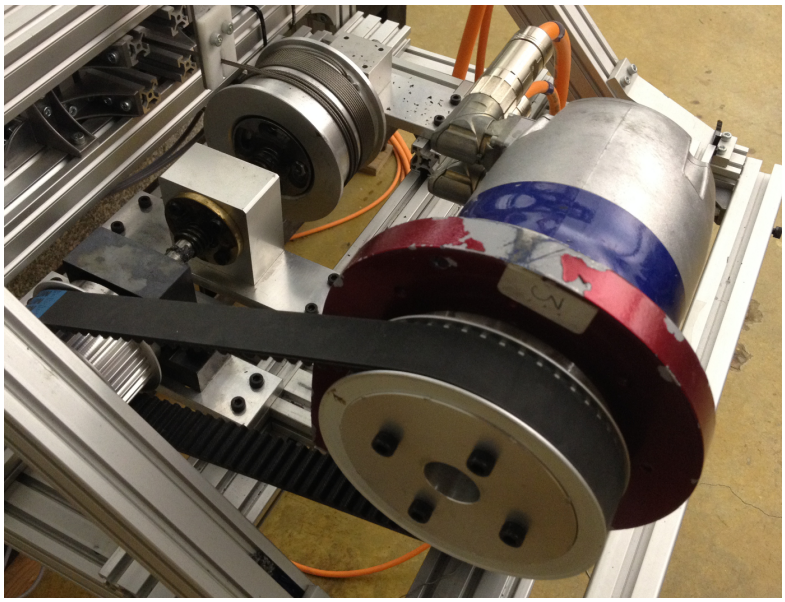

Figure 5.2: Motor-cable power transmission system

The specific locations of the mount points for the twelve cables are presented in Table 5.1 where $r_{c,i}$ and b_i are respectively the platform and frame mounts for the ith cable. This naming convention is consistent with the cable model presented in Section 3.1.2. The dimensions of Table 5.1 originate from the centre of the workspace which is considered to be the home position.

The cables used for the test setup are 1.6 mm diameter steel cables with a modulus of elasticity equal to 55 GPa. At the platform end, the cables are

Table 5.1: Warehousing robot cable mount locations

Cable Index	$r_{c,i}$ $[m]$			b_i $[m]$		
	x	y	z	x	y	z
1	0.152	0.048	0.065	1.50	0.500	0.000
2	0.232	−0.048	0.000	1.58	0.404	0.065
3	0.222	−0.017	0.087	1.50	−0.500	0.000
4	−0.222	−0.017	0.087	−1.50	−0.500	0.000
5	−0.232	−0.048	0.000	−1.58	0.404	0.065
6	−0.152	0.048	0.065	−1.50	0.500	0.000
7	0.152	0.048	−0.065	1.50	0.500	0.000
8	0.232	−0.048	0.000	1.58	0.404	−0.065
9	0.222	−0.017	−0.087	1.50	−0.500	0.000
10	−0.222	−0.017	−0.087	−1.50	−0.500	0.000
11	−0.232	−0.048	0.000	−1.58	0.404	−0.065
12	−0.152	0.048	−0.065	−1.50	0.500	0.000

attached with a spherical joint to allow for the rotational freedom required during motions. At the frame end, a set of rollers are used to ensure that the point and angle at which the cables are fed onto their respective spools is consistent. Figure 5.3 shows an example of both the rollers and the platform attached spherical joints.

For reasons that will be explained in Section 5.4, linear springs were added between the end of the cables and the platform for all four bottom cables. The stiffness constant for the added springs is equal to 753 N/m. Figure 5.3 (b) shows the bottom cable mount configuration with the series added springs.

5.2 Realtime Control Software

The system is powered by a Beckhoff CX2040 embedded PC. All software for the robot has been developed using a combination of Matlab and Simulink

(a) (b)

Figure 5.3: (a) Cable rollers (b) Cable-platform spherical joints

code, compiled as a realtime executable and run on the Beckhoff controller. A secondary control interface was also developed for communicating remotely with the realtime executable. The sampling time which the controller is operated at is $250\mu s$.

A screenshot of the Simulink block diagram for the realtime executable code is presented in Figure 5.4. There are five main subsystems which make up the realtime executable: Input handling, output handling, fault management, state management, and data collection.

The input handling block reads all of the raw sensor values, performs any necessary scaling and filtering, and combines all processed signals into a single input bus.

The state management block is where all high level control tasks are performed and it is responsible for switching between the various modes of operation. At any moment in time, the robot exists, uniquely, in one of the following states: halted, calibrating, homing, idle, and running program. In the halted state, all power and control is cut from the motors. The calibration and homing states are where the procedures of Section 5.6 are performed. In the idle state, the cable lengths are tensions are held constant. The running

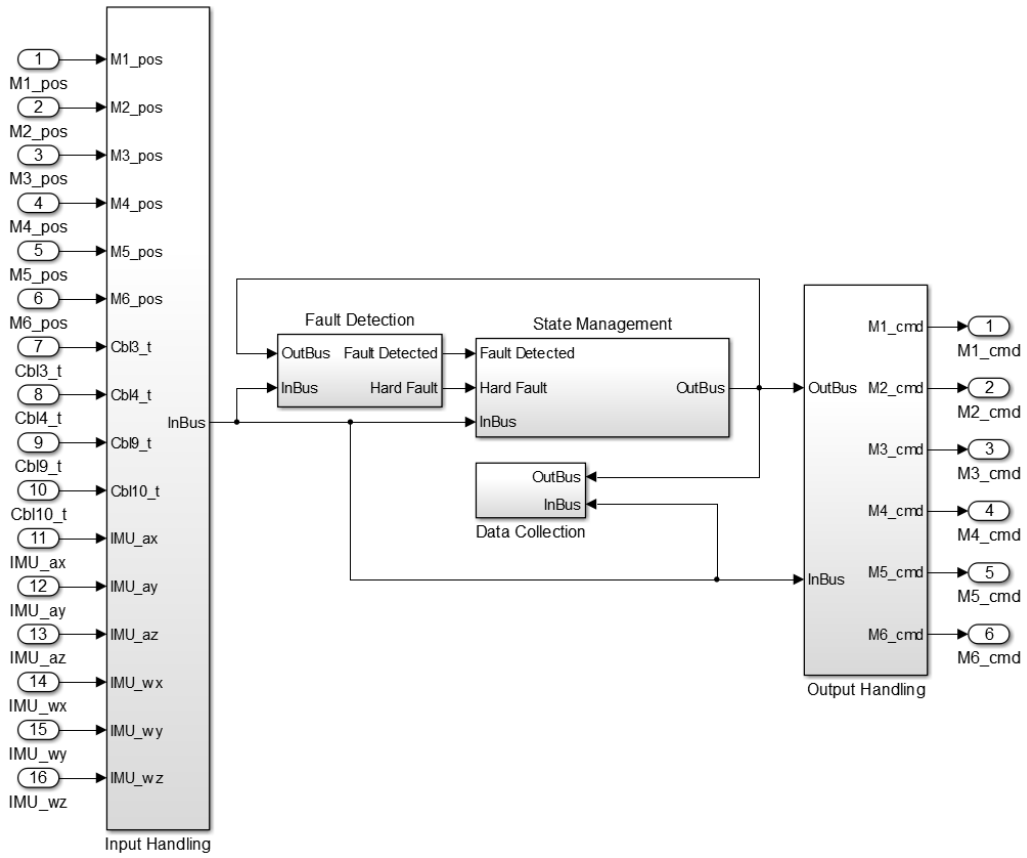

Figure 5.4: Realtime executable Simulink block diagram

program state is used to allow developers to implement their own experimental controller test procedures and embed them within the larger realtime executable. This simplifies the design for developers who only wish to test their controllers and provides an overall more stable and secure architecture.

The output bus signals generated from the high level controllers inside the state management block are then fed into the output handling block. The output handling block is where all of the low level motor controllers of Section 5.4 are contained. The position and tension commands contained on the output bus are converted to a set of motor toques by the lower level motor controllers and then sent to the motor drivers so the requested torques

may be applied.

The fault detection system was added to ensure the safety of the test setup and its operators. The fault management block is dependent on both the input and output buses and monitors the bus signals for anything unusual or concerning. If a fault is detected, a flag is raised by the fault management block and fed into the state management block, forcing a transition to a halted state. The fault detection system monitors for conditions such as violation of cable tension or length limits, violation of tracking error limits, sensor failure, and loss of communication with the control interface. In practice, the fault detection system was found to perform very well and has frequently saved the test setup from events which may have lead to catastrophic failure.

The data collection block simply logs all of the input and output bus signals to a file during the duration of the execution of a test program.

In order for a human operator to interact with and command the realtime executable to perform a desired set of tasks, a graphical user interface has been developed within Matlab and communicates with the Beckhoff controller over the Beckhoff hosted ADS bus. A screenshot of the user interface is provided in Figure 5.5. The interface is used to perform a number of functions for interacting with the robot: The buttons on the bottom left are used for controlling the state of the robot, the fields and buttons on the top left are used for setting up an automated build script which recompiles the realtime executable with a user supplied sub program embedded within it, and the text area on the right half of the interface is used to receive any diagnostic information from the realtime executable (such as information about any faults which have been triggered). In the background, the control interface is also used to relay camera data to the realtime executable for purposes of performing the calibration procedures discussed in Section 5.6.

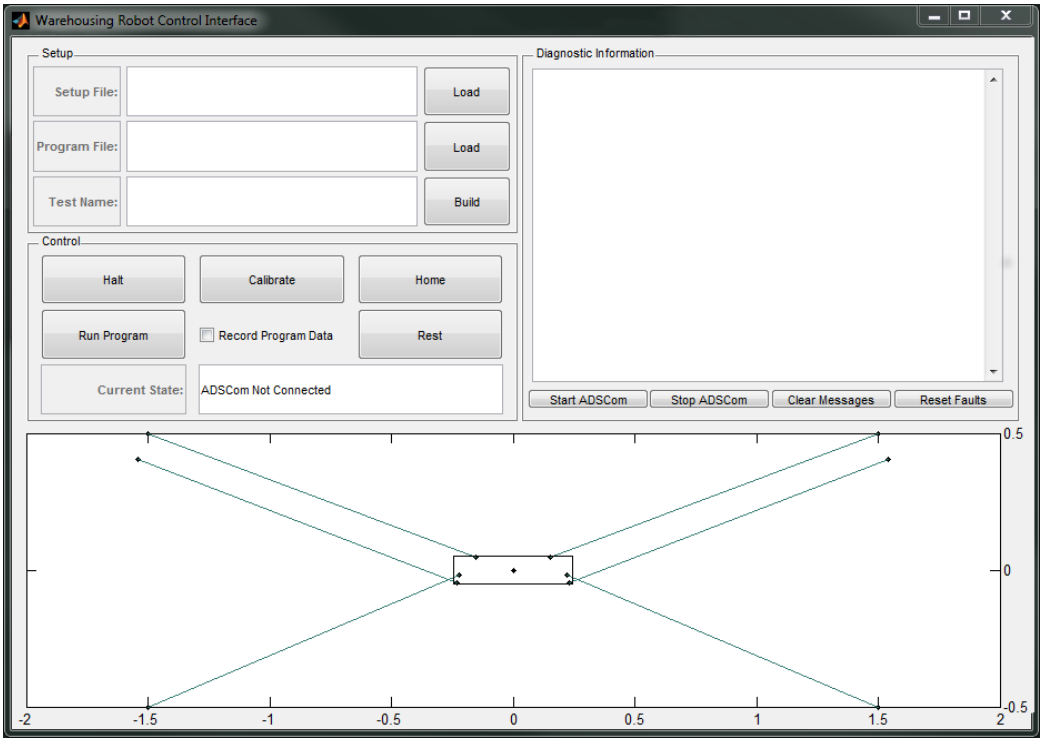

Figure 5.5: Graphical control interface for the realtime executable

5.3 Sensors and Instrumentation

Each of the four cable driving motors are equipped with high resolution resolvers. Since the motors used in this test setup are standard Beckhoff components, all of the necessary scaling, filtering, and signal processing required to produce a valid measure of the angular positions of the motors shafts is performed automatically by the Beckhoff control software: TwinCat.

Consider θ_i as the angular position of the ith motor and δl_i as the unstretched length of the cables driven by motor i. There exists an affine transformation $\delta l_i = m_i\theta_i + b_i$ where m_i can be found from analysis of the known gearing ratios and spool diameter of the power transmission system, shown in Figure 5.2. The offset b_i is determined by the initial conditions and must be calibrated for using the homing procedures described in Section

5.6. With the above transformation, the measured angular positions of the motor shafts can be transformed to a measure of the unstretched length of the driven cables. The reasoning behind why the measured length is stated as the unstretched length and not the true length of the cable comes from the fact that the change in length resulting from elongation of the cable between the spool and the platform is not accounted for. If you consider the cable as a spring with two fixed ends, one at the platform and one at the point where the cable exits the spool tangentially, any change in length of the cable resulting from elongation is imperceptible based on information of the spool position alone.

Since the effects of cable elongation are imperceptible directly from the available length measurements, In order to gain a sense of the vibration response of the platform, a 6-axis inertial measurement unit (IMU) has been added to the system and mounted approximately at the CG of the platform. The IMU consists of three orthogonal single axis accelerometers and three orthogonal single axis gyroscopes. The IMU produces an analog voltage output which is converted to a digital representation by an analog-digital converter (ADC).

The necessary scaling and offset parameters required to convert the output of the ADC to a more intuitive real-world unit representation were found by fitting experimentally measured values against a set of known true values using a linear least squares regression. For the accelerometers, data was collected using the gravitational acceleration vector as a known absolute reference. Static accelerometer data was recorded for a variety of poses such that each accelerometer would be aligned with the gravity vector and its inverse. Figure 5.6 shows the fitting results for the three accelerometers.

Fitting data for the gyroscopes was obtained by securing the IMU to one of the pendulum actuators (shown in Section 5.5) and oscillating the pendulum at a known rate. Figure 5.7 demonstrates how the system was setup for collecting the gyroscope calibration setup.

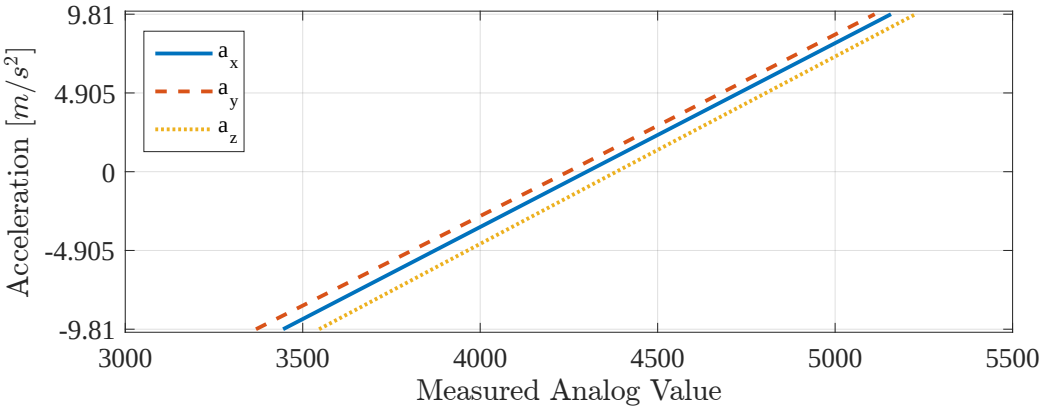

Figure 5.6: Accelerometer parameter identification data fitting

Similar tests were performed along the three rotational axes and for various excitation references to verify the identification calibration parameters were consistent. Once all data had been collected, a least squares regression was performed to identify the scaling parameters for each gyroscopic axis. Figure 5.8 summarizes the results where w is the true angular velocity of the motor shaft and $\hat{w}$ is the angular velocity predicted by the calibrated gyroscope model.

For purposes of measuring cable tensions, load cells were added in series with each of the four bottom cables. The load cells were powered and their output processed via a Beckhoff strain gauge interface card (EL3356-0010). The Beckhoff TwinCat software contains procedures for automatically calibrating the signal output from the load cells given the manufacturer data, specific to the individual load cells, and this procedure was applied for converting the analog voltage outputs of the load cells to a force representation in Newtons.

The motors used for the pendulum actuators make use of absolute encoders and so no special fitting or homing procedures were necessary for their application. The absolute encoders produce a consistent measure of angular position of the motor shafts.

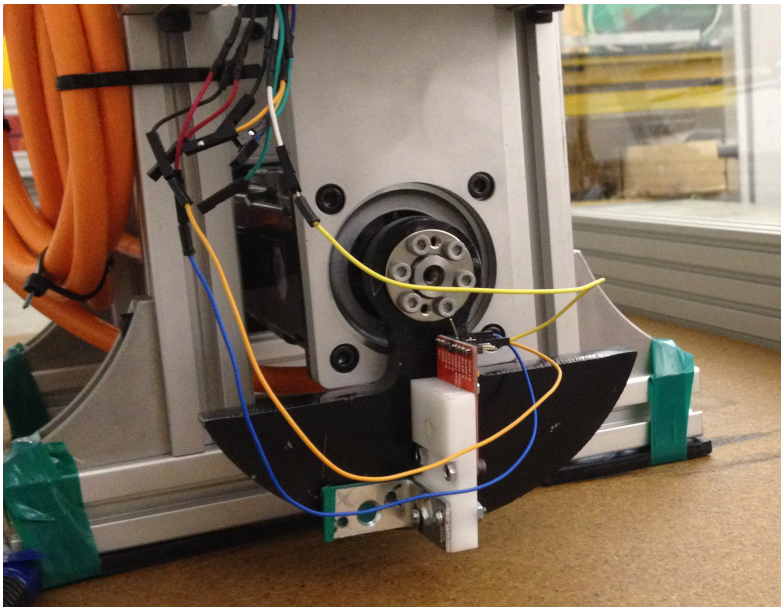

Figure 5.7: Gyroscope calibration apparatus

5.4 Motor Control

For the active vibration controllers of Chapter 4, it is assumed that the cable unstretched lengths are directly controllable. Obviously this is not the case in reality. Instead, an inner loop of low-level motor controllers are used to track the cable unstretched length commands produced by the high-level task space controller.

In total there are four motors: two in the top corners and two in the bottom corners. Each motor is equipped with a high resolution resolver which is used for measuring the angular position of the motor shaft. Given that the gearing ratio of the transmission system is known and the diameter of the cable spools are known, a change in angular position of the motor can easily be transformed to the change in length of the cables.

The top motors are operated in position control mode and track a commanded unstretched length for the cables. The type of controller used for

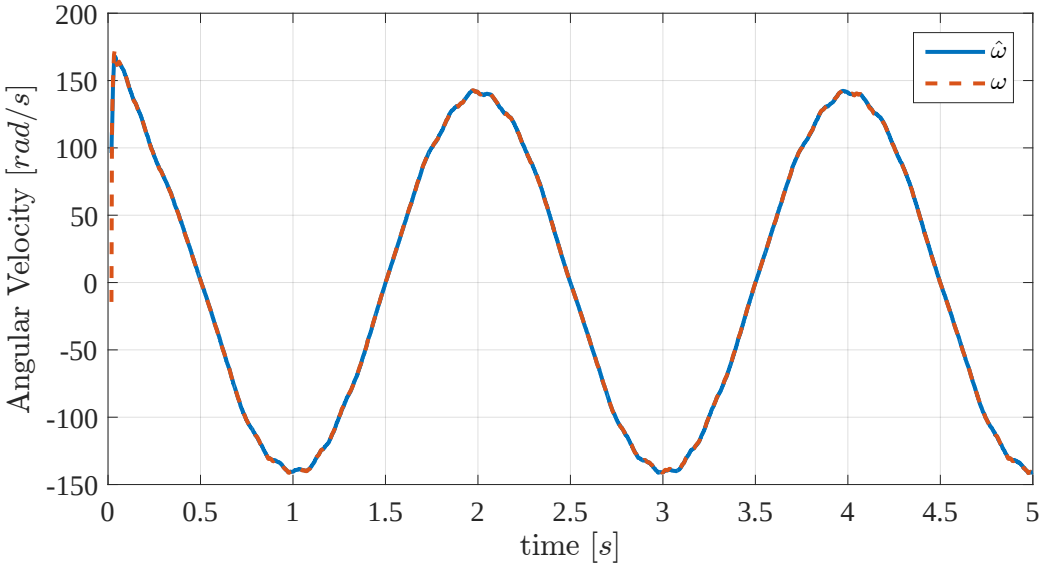

Figure 5.8: Gyroscope parameter identification data

controlling the upper motors is a simple PID controller with saturation where the motor resolvers are used for position feedback. Figure 5.9 shows a block diagram of the controller topology used for the upper motors where $G(s)$ represents the motor plant and the control signal u, which corresponds to the applied motor torque, is saturated before it is applied.

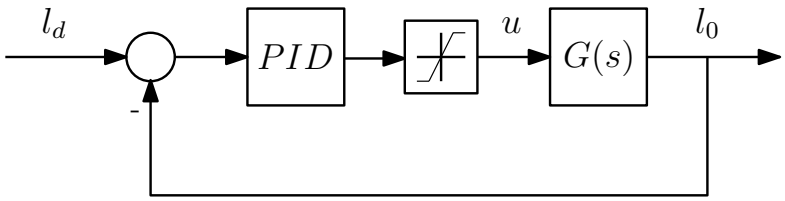

Figure 5.9: Upper motor control topology

The PID gains for the upper motors were tuned experimentally until an acceptable level of performance was obtained. Figure 5.10 shows the typical tracking performance of the upper motors while following a reference trajectory. The tracking error for the cable lengths has generally been observed to

be sub-millimeter. Based on the high-level of performance which has been achieved for cable length tracking of the upper motors with the designed motor controllers, it can be argued that the assumption of direct cable length controllability employed by the high-level task-space controllers is reasonable and valid.

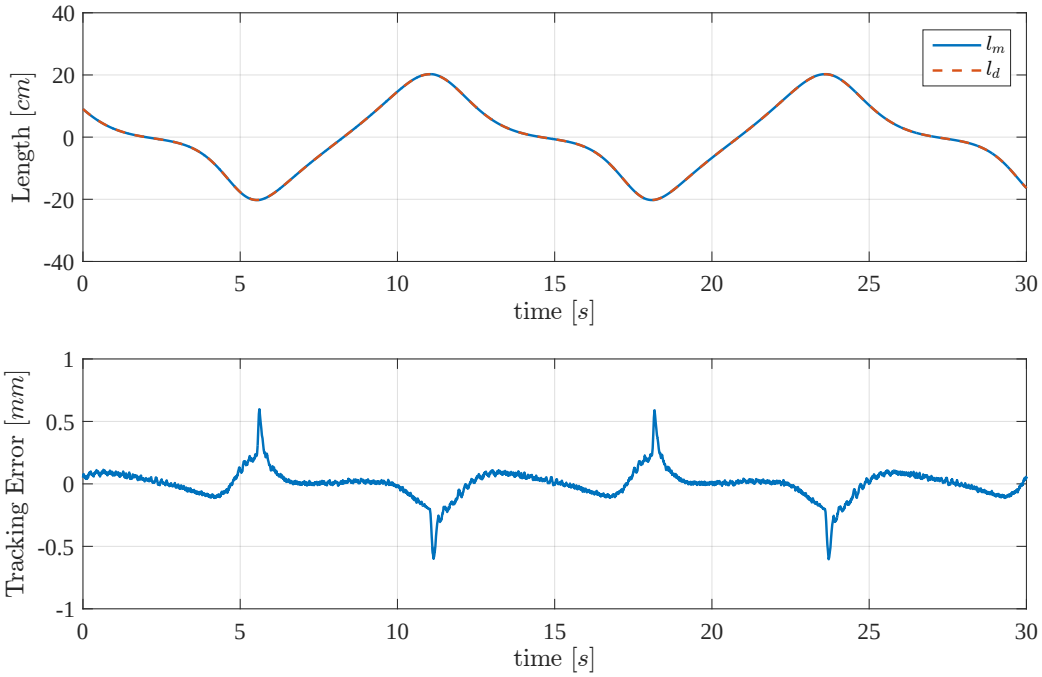

Figure 5.10: Upper motor position tracking performance

The lower motors use the same high resolution resolvers as the upper motors. Additionally, each of the four bottom cables have a load cell attached in series between the cable and the mobile platform which is used for measuring the tensile forces in the axial direction of the cables. In contrast to the upper motors, the lower motors are operated under force control. The motivation behind using force control for the lower motors is to account for any errors in the inverse kinematic model. Unless the inverse kinematic and elastic properties of the cables are known perfectly, using only length control for all cables provides no guarantee for the internal forces of the manipulator.

Originally, a simple PID controller using cable tension information from the load cells for feedback was developed. However, because the cables used in this setup are fairly stiff, it is very difficult to obtain good force tracking performance using this strategy. a position error of $1mm$ in the unstretched length of the cables results in a difference in force of roughly $220N$. This requires the force controllers to be very aggressive and have very high gains. Another issue is that the measured load cell signals are extremely noisy (see Figure5.12), to the point where no useful level of derivative feedback could be applied. The combination of these two factors makes it very difficult to stabilise the system while still maintaining a high level of precision in control.

Another difficulty, or even danger, with using a simple pure force feedback arises from the possibility of cables becoming slack. In such a state, the measured tensions will be essentially zero and continue to read zero until all of the slack has been pulled from the cable. Meanwhile, the force controller will try to eliminate the large force tracking error, its integral terms will wind up, and the cable will be wound up onto its spool very aggressively. As soon as the cables run out of slack and are put under tension, it will result in a vary large mechanical shock from the large resulting impulse.

To deal with the identified challenges of implementing a direct force feedback controller, two different approaches have been applied to ensure precise and stable tracking: linear springs with a known stiffness constant were added in series with the cables to increase the compliance of the system, making it less sensitive to disturbances and minor position errors, and a hybrid position-force feedback control strategy was used.

The topology for the hybrid control strategy is presented, as a block diagram, in Figure 5.11 where $G(s)$ represents the motor plant dynamics and k_s is the stiffness constant for the linear springs added in series with the cables.

The main idea behind the hybrid topology is to supply a position feedback controller with a modified length reference which is predicted to produce a

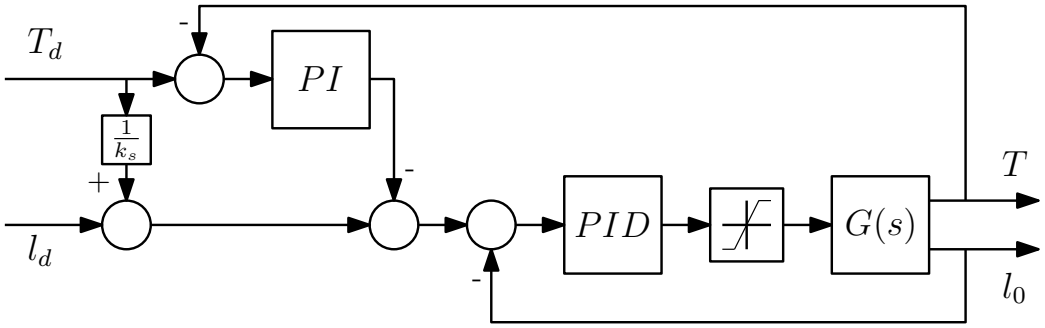

Figure 5.11: Lower motor control topology

desired cable tension. A secondary feedback loop based on the measured force error from the load cells is added to correct for any tension errors resulting from imperfections in the length predictions. The output of the force feedback loop is added to the desired length reference before it is fed into the position controller to act as a reference correction term.

Based on the known geometry of the robot, the cable lengths at a desired platform position can be determined using the inverse kinematics procedure of Section 4.1.2. Since the stiffness constant, k_s, of the series added linear springs is known, for a given cable tension, T, the elongation of the spring, δx, is determined by Hook's law:

$$T = k_s \, \delta x \tag{5.1}$$

The stiffness of each cable is far lower than that of the in series springs. Accordingly, the elongation of the cables in comparison with the elongation of the springs will similarly be far lower, to the point where for this system it can be safely ignored. For a desired cable tension, T_d, at a given platform position, the modified length reference, l_d, becomes:

$$
\begin{aligned}
l_d &= l_0 + \delta x \\
l_d &= l_0 + (\frac{T_d}{k_s})
\end{aligned}
\tag{5.2}
$$

where l_0 is the length of the cable at the given position, assuming no elongation. The desired length reference is modified further by adding the correction term generated by the force feedback loop and then finally fed into the position feedback loop.

A display of the typical tracking performance which has been observed for the hybrid controller following a desired cable tension trajectory is presented in Figure 5.12. Tracking errors have been generally found not to exceed $10N$.

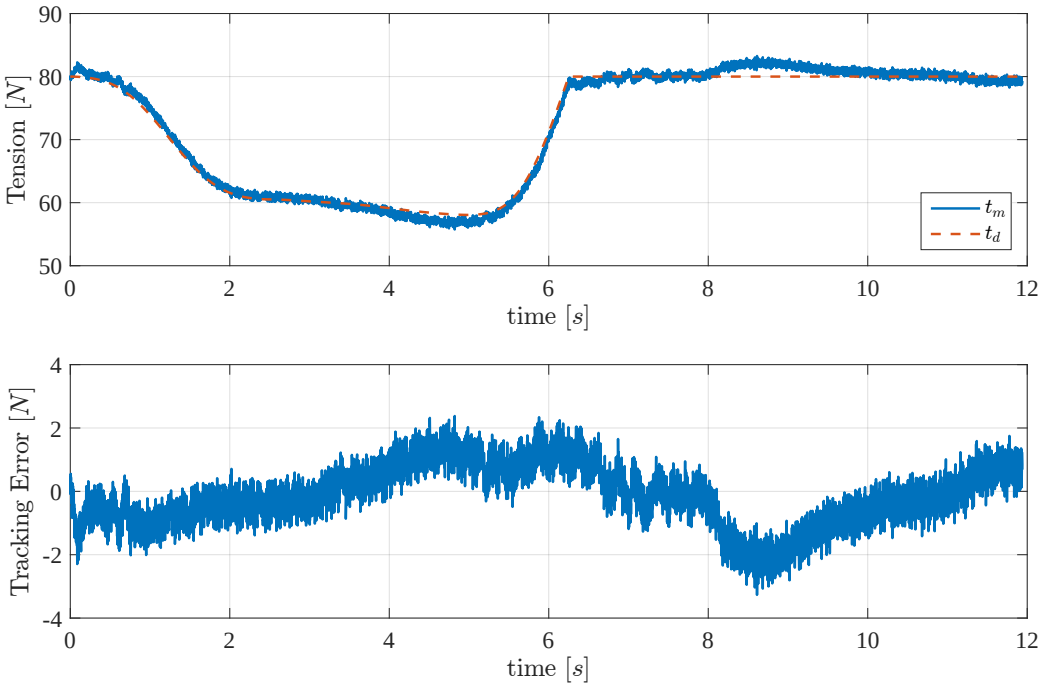

Figure 5.12: Lower motor force tracking performance

5.5 Pendulum Actuator

Two identical pendulum actuators were designed and built as part of the requirements of the multi-axis reaction system introduced in Chapter 3. Each actuator consists of a direct drive DC motor with absolute encoders, a mount plate, pendulum shaped load mass, and a coupler to fix the load mass to the motor shaft. Each motor is capable of producing $1.3Nm$ of torque. Figure 5.13 provides a CAD model of the mobile platform with two of the pendulum actuators attached. The dimensions and spacing present in the actuator design was chosen to adapt to the size and shape of the motors which were available. It was important for the sake of flexibility and safety that the pendulum shaped load mass be able to swing fully without any chance of collision with the mobile platform or cables.

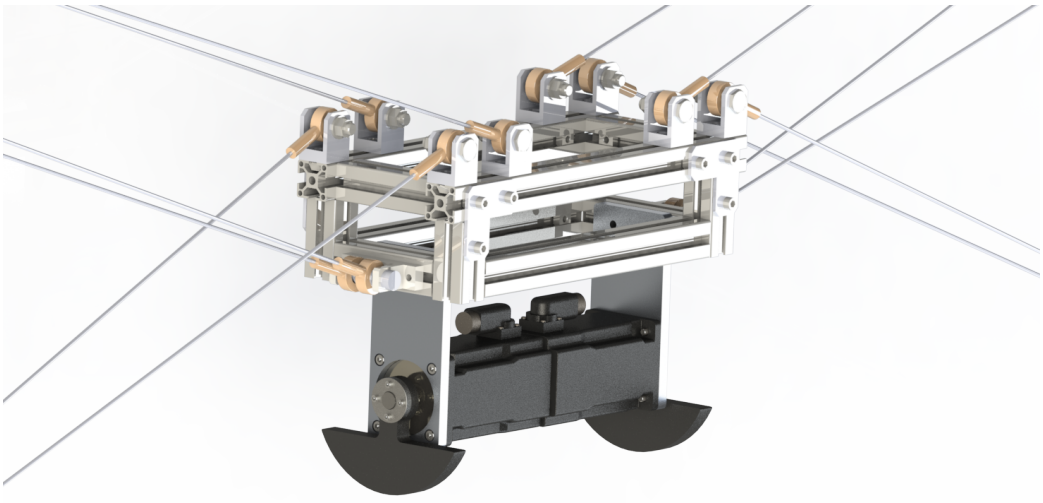

Figure 5.13: Platform mounted pendulum actuator CAD Model

The load masses (shown in Figure 5.14) were fabricated out of steel, each having a mass of $640g$. The shape of the mass was designed to keep the centre of mass as low as possible while still guaranteeing that there would be no chance of a collision with the mobile platform.

Figure 5.15 provides a close up view of the warehousing robot mobile

Figure 5.14: Pendulum load mass CAD Model

platform after fabrication and integration of the pendulum actuators was performed.

5.6 Homing Procedures

Since the motors that drive the system lack any form of absolute position reference, the zero reference for the resolvers must be recalibrated each time the system is reset. For this purpose, two visions systems are employed.

When the system is turned off, all of the cables loose tension. When the cables are slack, the resolver measurements used to estimate the unstretched lengths of the cables cannot be assumed to be correct as the position of the spool does not necessarily correspond to the length of the cable in that state. In order for the zero reference of the resolvers to be reset, the slackness must first be taken out of the cables. In order to do this safely, a camera is used to track the position of the mobile platform within the workspace.

Four coloured markers are attached to the fixed frame and two are attached to the mobile platform. Using colour thresholding and blob analysis,

Figure 5.15: Platform mounted pendulum actuator prototype

the locations of the 6 markers within the image frame can be determined. Figure 5.16 shows the robot with the 6 red markers and the resulting color thresholded image. Since at all times the mobile platform is located within the confines of its fixed frame, the markers which correspond the platform can be identified by sorting the six markers in terms of their vertical components and taking the middle two markers

Once the location of the four frame markers are known, the centre of the workspace can be calculated by finding the geometric center of the four points. Similarly, the location of the platform can be calculated by finding the midpoint between the two corresponding markers.

Using the inverse kinematic model (Section 4.1.2), the cable lengths at the workspace centre and current position can be calculated. The required change in length can then be calculated by subtracting the centre point length

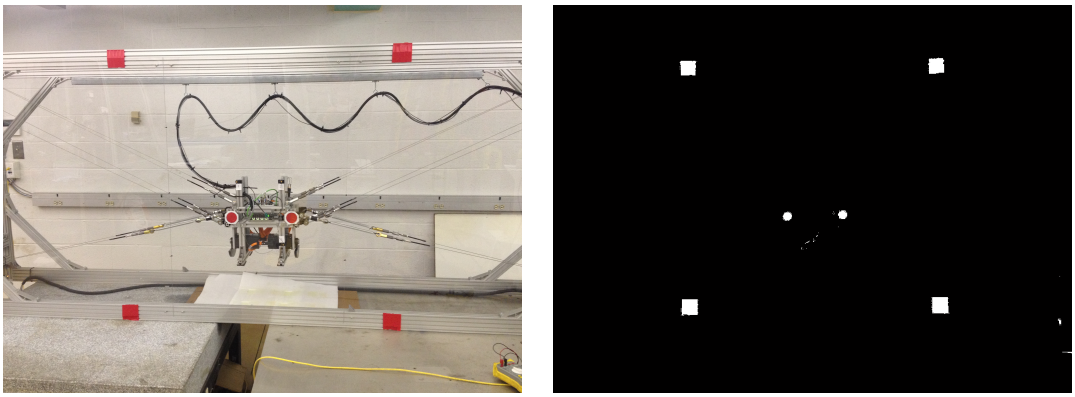

(a) (b)

Figure 5.16: (a) Front view of setup with markers attached (b) color thresholded image used for tracking

from the current length. This required change in length is used as a reference for the motors which, based on this error, slowly work to tension the cables and move the platform towards its homing position.

Once the platform is within a certain threshold distance from the workspace centre and the cable tensions are within an acceptable range, calibration is deemed complete and the resolver zero reference offsets are updated based on the current known position. For additional refinement, a secondary high precision vision system is used for fine tuning the calibrated zero reference points.

Chapter 6

Experimental Results

In order to investigate the effectiveness of the multi-axis vibration control system designed in Chapter 4, a set of experiments were performed using the experimental setup described in Chapter 5.

The primary motivation behind the design of the chosen test procedures is to demonstrate the effectiveness of the controllers at eliminating end effector vibrations. The robustness features of the controllers are also investigated by varying the mass of the end effector and observing any resulting change in performance.

The experiments were divided into two main categories which aim individually evaluate the in-plane and MARS controllers. The results obtained from the performed experiments and related discussion of the results are presented in sections 6.1 and 6.2 for the in-plane and MARS controllers respectively.

6.1 In-Plane Control

The maneuver chosen for testing the in-plane controllers is to trace a rectangle, centered at the home position, with a width of 30cm and height of 10cm. The maneuver is performed such that the platform both starts and ends at the home position. Specifically, the sequence of motions to perform

the maneuver are: start from the home position, move 5cm downwards, 15cm to the right, 10cm upwards, 30cm to the left, 10cm downwards, 15cm to the right, 5cm upwards to return to the home position, ending the motion. The top speed for each of the motion segments is 15cm/s. The maneuver was maintained constant across all tests performed to ensure the dynamic conditions are consistent when comparing the system natural response with the active damping performance of the vibration controller.

Two different testing conditions were considered: the case where no additional load mass is added, and the case where a 6kg load mass is added to the platform. Figures 6.1 and 6.2 show the traced position of the platform during the maneuver for the no load and added load cases respectively. The figures also demonstrate the tracking behavior of the system with the active vibration controller active and disabled.

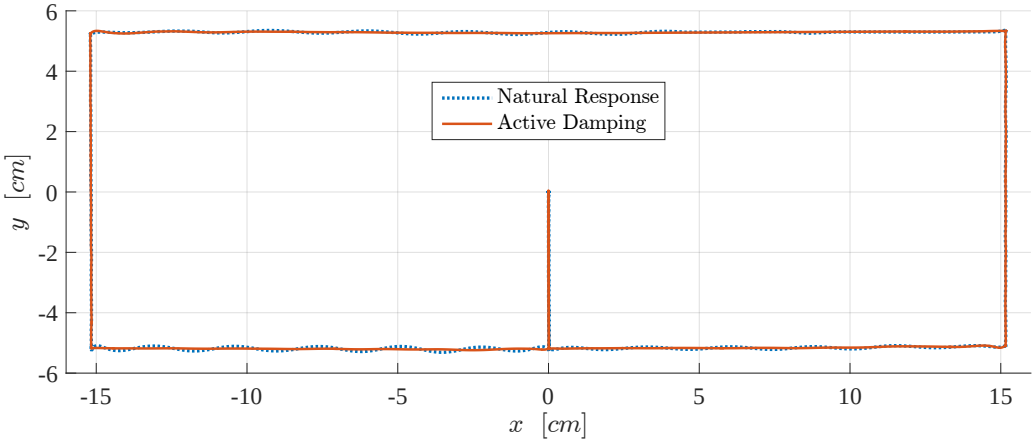

Figure 6.1: Trajectory tracking performance with no load mass

In all cases, the platform does a good job at tracking the reference trajectory. However, in the case where active vibration controller is disabled, it is clearly observable that the platform experiences some oscillatory motion in the vertical direction. With the added load, the amplitude of the oscillations increases. By enabling the active vibration controller, in both the no load

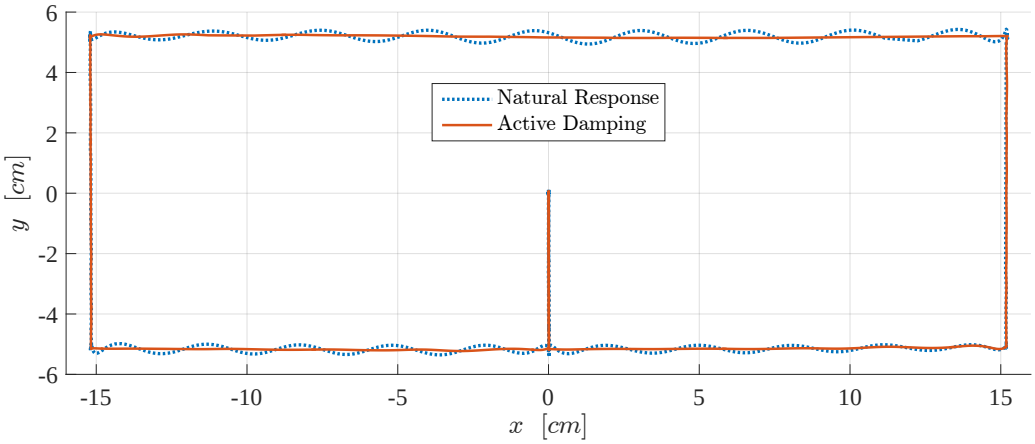

Figure 6.2: Trajectory tracking performance with added load mass

and added load cases, the observed oscillations are effectively eliminated.

The vertical acceleration of the platform during the motions along with the control inputs corresponding to the desired cable tensions is presented in Figures 6.3 and 6.4. It is interesting to note the amount of force compensation required to solve the vibration problem is quite low (< 5N). It is also interesting to note that the control signals are effectively saturated at various points during the motion, demonstrating the procedure for limiting cable tensions outlined in Section 4.1.5.

6.2 Out-Plane Control Using MARS

In order to fairly compare the natural system damping with the response of the system using MARS, it is necessary to ensure that the initial conditions are consistent between tests. To achieve this, each test consists of two phases: a swing-up phase and a damping phase.

During the swing-up phase, both pendulums are operated in position control mode and fed an equivalent sinusoidal reference. The frequency of the sinusoidal reference was tuned to match the natural frequency of the

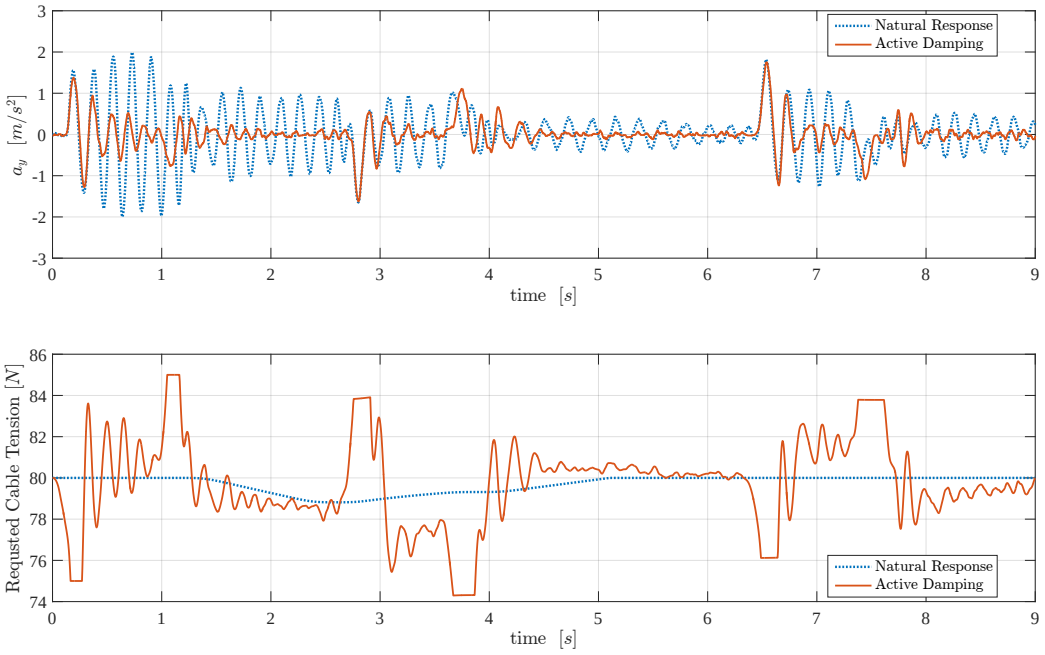

Figure 6.3: Vertical acceleration during trajectory with no load mass

mobile platform in the out of plane translational direction. Swinging the pendulums at the natural frequency causes the platform to similarly swing in and out of its equilibrium plane.

For the natural response case, the pendulums are held at a constant of 0 degrees. For the active damping case, the Hierarchical sliding mode controller presented in 4.2 was used. Figure 6.5 demonstrates the two phase motion generated and confirms that the initial conditions at the beginning of the natural and active damping cases are indeed identical. For the first three seconds of the motion, the pendulums are operated in position control mode to excite the platform in the out of plane direction. Then, after three seconds, the controllers switch and the pendulums are either held at 0 degrees or the active damping controllers are applied, depending on the test condition. To highlight the damping phase, which is the area of primary interest, the swing up phase has been discarded from the results presented in the remaining

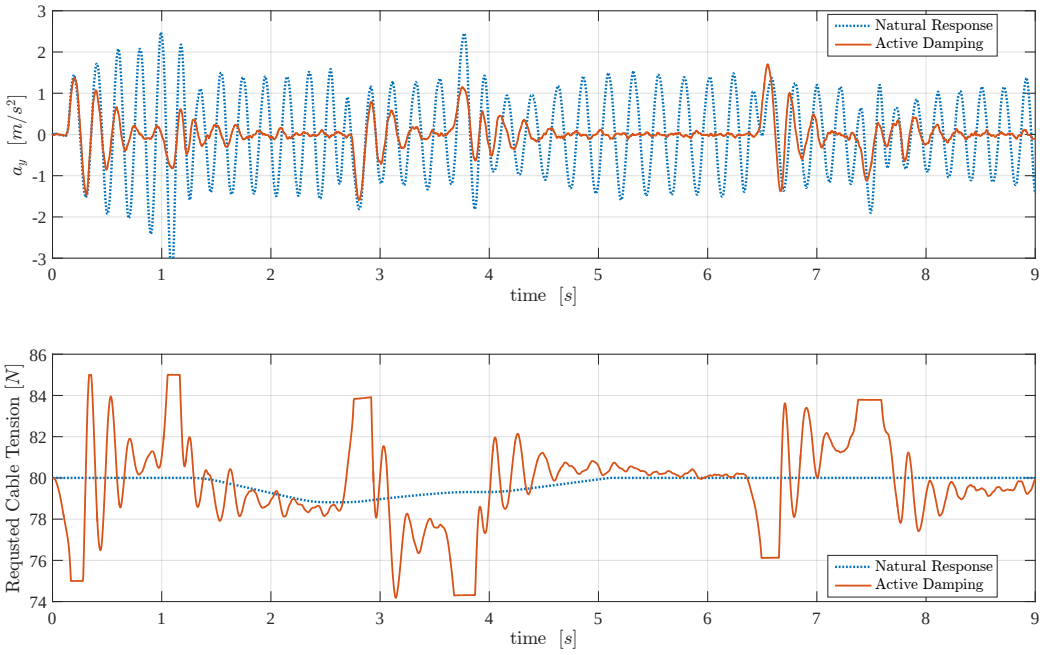

Figure 6.4: Vertical acceleration during trajectory with added load mass

figures and time is shifted such that the damping phase begins at time $t = 0$.

Figure 6.6 shows the effect of the Hierarchical sliding mode controller of Section 4.2 for controller z, θ_x, and the angular position of the two pendulums. Clearly the proposed active damping mechanism and controller work very well at eliminating the out of plane oscillatory displacements. Experimental results for the damping of vibrations in the θ_y direction could not be obtained. Because of the high stiffness of the system and the presence of unmodeled damping forces, any excitation of the vibratory modes in the θ_y direction which could be generated would be very rapidly damped before the controller could have any observable effect.

Insensitivity to variations in mass is in important property for the controller, considering its intended application of pick and place operations. Figure 6.7 shows the active damping performance with and without an additional 6kg load mass added to the platform. In both the loaded and unloaded

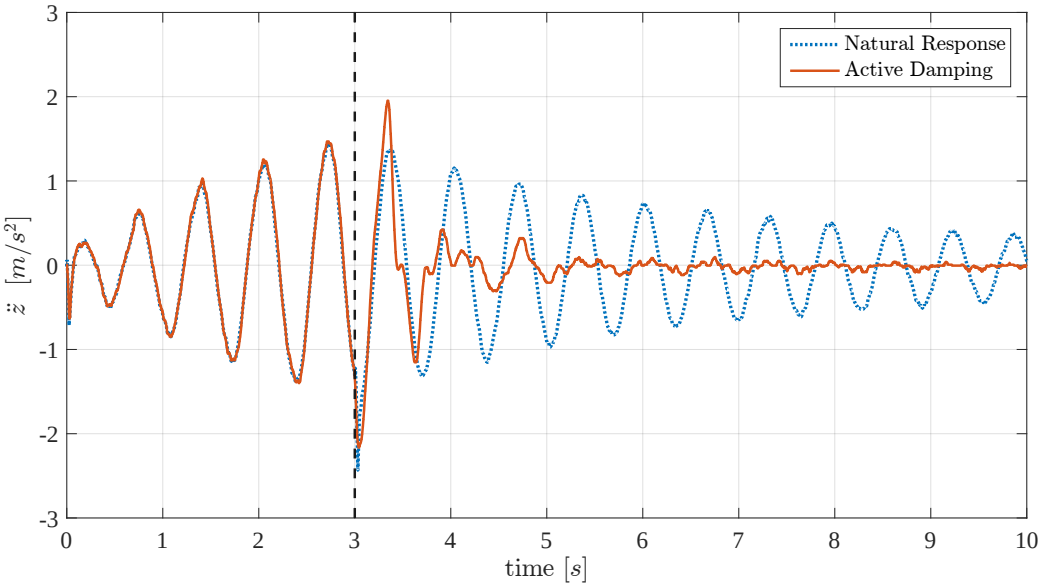

Figure 6.5: Swingup phase used for generating out of plane excitations

cases, the controller produces similar performance, is stable, and provides a significant improvement over the natural damping present within the system.

Since the out of plane dynamics of the platform are dependent on the position of the platform within the plane, the tests were performed at various locations across the workspace. Figure 6.8 shows the active damping performance for the mass loaded platform at various positions. Clearly the out of plane response can vary significantly depending on the location of the platform. However, in all cases tested, the system remains stable and the active damping controller provides a significant improvement over the natural response.

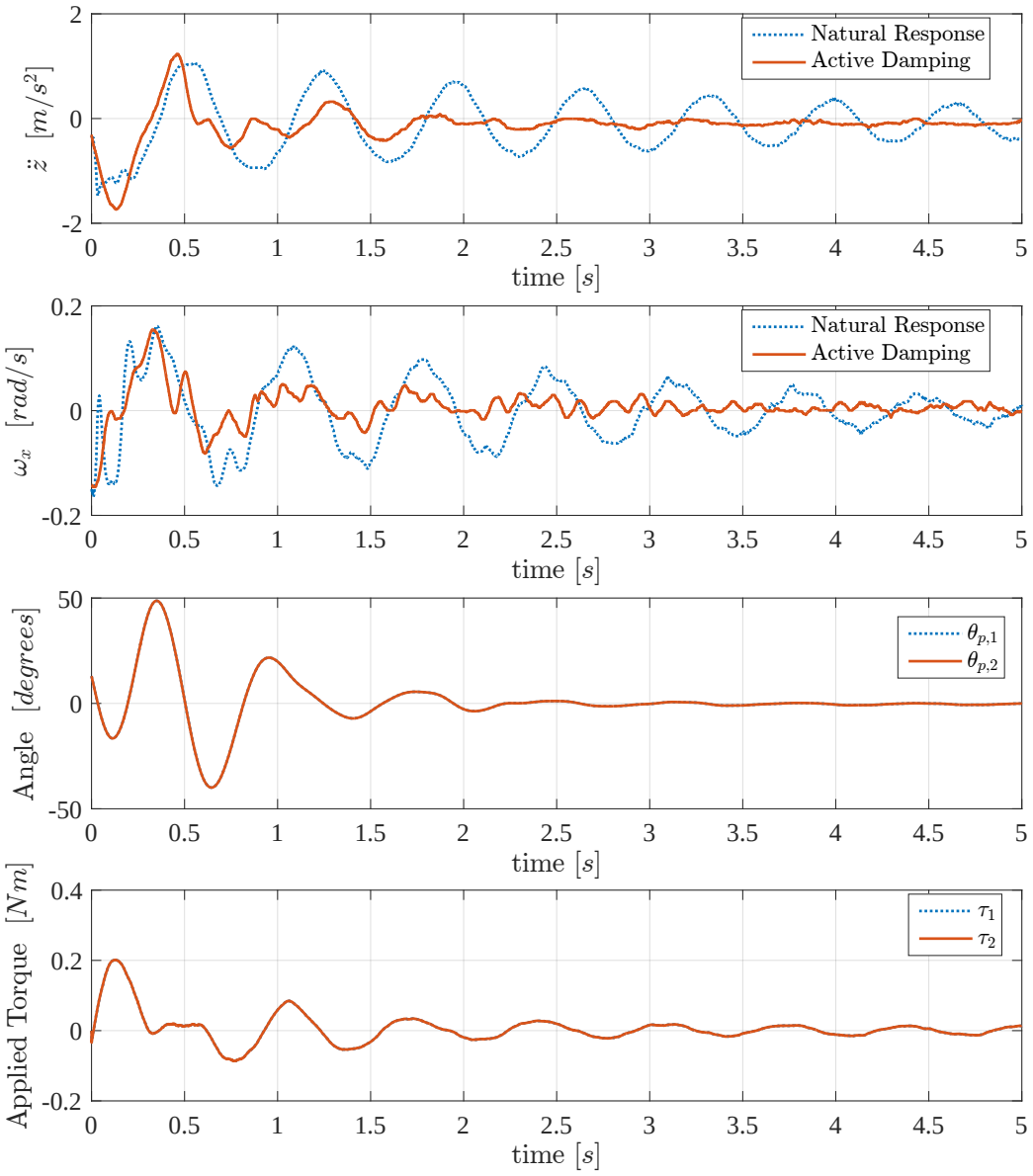

Figure 6.6: Multi axis damping performance of MARS

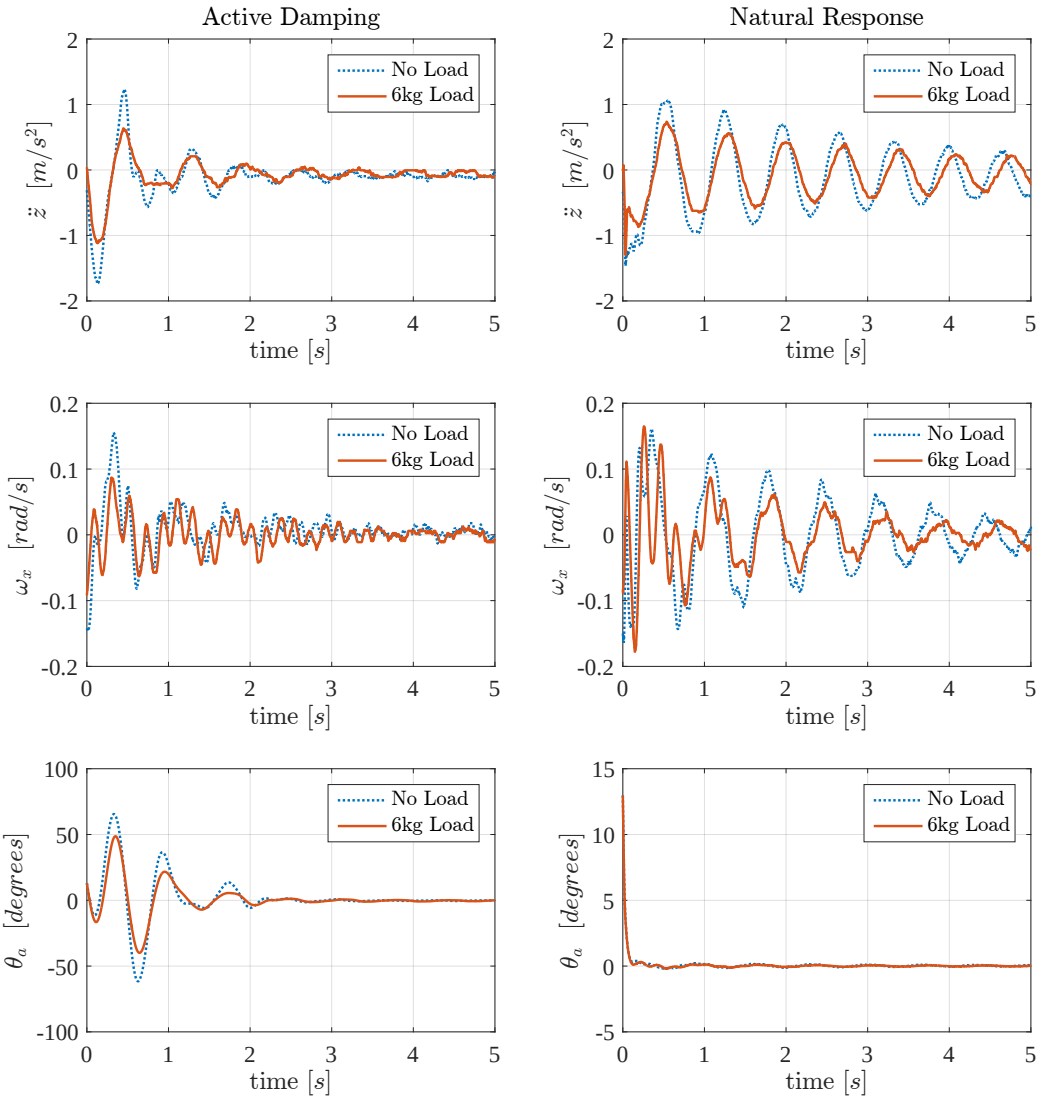

Figure 6.7: MARS performance with varied load

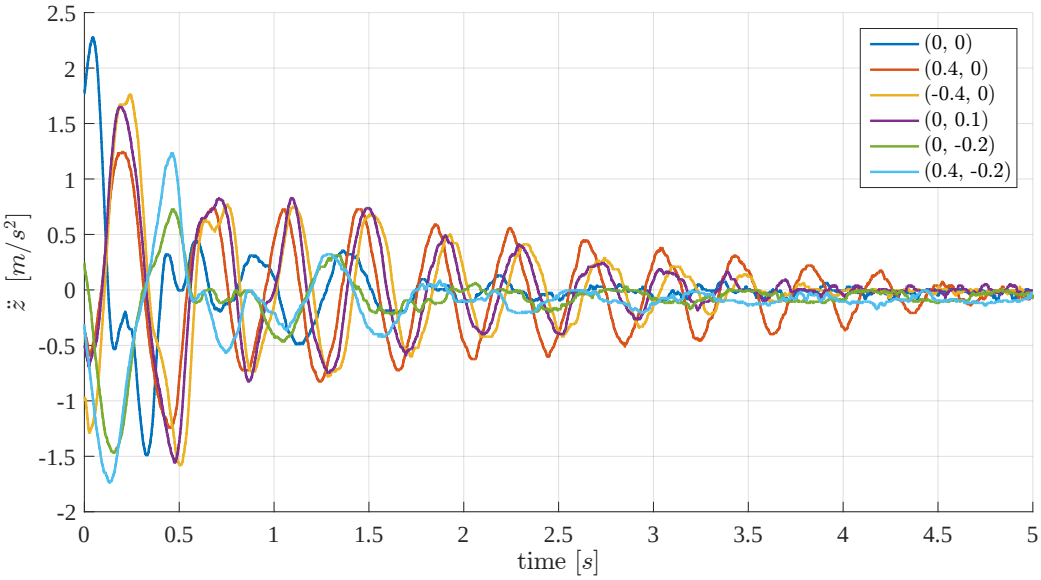

Figure 6.8: MARS performance with varied platform position

Chapter 7

Conclusions and Future Work

Cable driven parallel robotic manipulators have great potential in applications where low cost or high accelerations are necessary. In order for cable driven manipulators to become viable for industrial application however, the issue of low manipulator stiffness and vibrations resulting from cable elongation and cable unidirectional load tolerance must be solved.

A planar cable driven manipulator design, intended for warehousing type applications, has been studied and used as the focus for developing a complete active vibration control system. Using a developed six degree of freedom dynamic model, it was shown that planar cable driven robots are uncontrollable in three of the six spatial degrees of freedom. The uncontrollable modes correspond to the directions that cause the mobile platform to deviate from its equilibrium plane. Specifically, rotation about the two planar axis and translation along the planar normal axis cannot be controlled using cable actuation alone.

In order to solve the problem of the existence of uncontrollable modes and bring the system into a state of full controllability, a multi-axis reaction system (MARS) has been developed. The proposed system consists of two rigid pendulum actuators. By exploiting the inherent coupling in the platform dynamics, it is possible, despite being underactuated, to eliminate vibrations

in the three uncontrollable directions while requiring only an additional two actuators.

A set of decoupled PD controllers are proposed for eliminating vibrations within the plane resulting from cable elongation. The controllers use acceleration data, taken from an IMU mounted at the end effector, to modify the desired tensions and length commands for the cables.

Due to the nonlinear nature of pendulum dynamics and desire for robustness in control, a hierarchical sliding mode controller is presented for controlling the MARS and regulating the non-planar modes.

Using a multibody dynamic model, developed in MapleSim and exported to Simulink, both the in plane and out of plane controllers were shown to perform well.

Experimental results were presented which demonstrate the actual performance of the MARS on a planar cable driven robotic manipulator. Both the developed in plane and out of plane controllers were implemented and shown to perform very well.

7.1 Future Work

An important next step for purposes of further validating the results of this thesis is to build a full scale prototype of the studied cable driven warehousing robot. Due to its small size and the relatively high stiffness of the cables used, it was very difficult to induce any vibrations of a considerable amplitude in certain directions. This limitation prevented the testing of the developed vibration control system performance in certain directions.

Another consideration is the mass of the cables. In this study, because the length of the cables was relatively short, the cables could be modeled as massless straight line segments without much loss in performance. In a warehousing application, cable lengths could possibly be on the order of 50-100m. At such lengths, the weight of the cables relative to internal tension

forces would become quite substantial. It is therefore important to study what affect cable weight has on controller performance and design. At such lengths as well, the magnitude of elongation in the cables would be far more significant, making the proposed vibration control system more necessary and valuable.

Limitations of the employed test setup aside, it is believed that the actuator design proposed in this thesis can be used as an effective, low cost, and easily integrated solution for eliminating any induced vibrations in the uncontrollable modes of planar systems.

While the scope of this study has been limited to fully-constrained cable driven parallel robotic manipulators, it is suspected that the actuator and control method designed in this thesis likely have potential applications extending far beyond the single class of systems investigated.

Bibliography

[1] Sergio Torres-Mendez and Amir Khajepour. Design optimization of a warehousing cable-based robot. In *ASME 2014 International Design Engineering Technical Conferences and Computers and Information in Engineering Conference*, pages V05AT08A091–V05AT08A091. American Society of Mechanical Engineers, 2014.

[2] Xiaoqiang Tang. An overview of the development for cable-driven parallel manipulator. *Advances in Mechanical Engineering*, 6:823028, 2014.

[3] Clément GOSSELIN. Cable-driven parallel mechanisms: state of the art and perspectives. *Mechanical Engineering Reviews*, 1(1):DSM0004–DSM0004, 2014.

[4] Sadao Kawamura, Won Choe, Satoshi Tanaka, and Shunmugham R Pandian. Development of an ultrahigh speed robot falcon using wire drive system. In *Robotics and Automation, 1995. Proceedings., 1995 IEEE International Conference on*, volume 1, pages 215–220. IEEE, 1995.

[5] Robert Dekker, Amir Khajepour, and Saeed Behzadipour. Design and testing of an ultra-high-speed cable robot. *International Journal of Robotics & Automation*, 21(1):25, 2006.

[6] Daniel R Altschuler. The national astronomy and ionosphere center's (naic) arecibo observatory in puerto rico. In *Single-Dish Radio Astronomy: Techniques and Applications*, volume 278, pages 1–24, 2002.

[7] Rendong Nan, Di Li, Chengjin Jin, Qiming Wang, Lichun Zhu, Wenbai Zhu, Haiyan Zhang, Youling Yue, and Lei Qian. The five-hundred-meter aperture spherical radio telescope (fast) project. *International Journal of Modern Physics D*, 20(06):989–1024, 2011.

[8] Mohammad A Khosravi and Hamid D Taghirad. Robust pid control of fully-constrained cable driven parallel robots. *Mechatronics*, 24(2):87–97, 2014.

[9] Robert L Williams Ii and Paolo Gallina. Translational planar cable-direct-driven robots. *Journal of Intelligent and Robotic systems*, 37(1):69–96, 2003.

[10] Robert L Williams, Paolo Gallina, and Jigar Vadia. Planar translational cable-direct-driven robots. *Journal of Robotic Systems*, 20(3):107–120, 2003.

[11] Mohammad A Khosravi and Hamid D Taghirad. On the modelling and control of fully constrained cable driven robots with flexible cables. In *Control, Instrumentation and Automation (ICCIA), 2011 2nd International Conference on*, pages 1030–1035. IEEE, 2011.

[12] Y Babazadeh Bedoustani, Hamid D Taghirad, and Mohammad M Aref. Dynamics analysis of a redundant parallel manipulator driven by elastic cables. In *Control, Automation, Robotics and Vision, 2008. ICARCV 2008. 10th International Conference on*, pages 536–542. IEEE, 2008.

[13] Jingli Du, Hong Bao, Chuanzhen Cui, and Dongwu Yang. Dynamic analysis of cable-driven parallel manipulators with time-varying cable lengths. *Finite Elements in Analysis and Design*, 48(1):1392–1399, 2012.

[14] Xiumin Diao and Ou Ma. Vibration analysis of cable-driven parallel manipulators. *Multibody system dynamics*, 21(4):347–360, 2009.

[15] Clement Gosselin. Stiffness mapping for parallel manipulators. *Robotics and Automation, IEEE Transactions on*, 6(3):377–382, 1990.

[16] Saeed Behzadipour and Amir Khajepour. Stiffness of cable-based parallel manipulators with application to stability analysis. *Journal of mechanical design*, 128(1):303–310, 2006.

[17] Sadao Kawamura, Hitoshi Kino, and Choe Won. High-speed manipulation by using parallel wire-driven robots. *Robotica*, 18(01):13–21, 2000.

[18] Pooneh Gholami, Mohammad M Aref, and Hamid D Taghirad. On the control of the kntu cdrpm: A cable driven redundant parallel manipulator. In *Intelligent Robots and Systems, 2008. IROS 2008. IEEE/RSJ International Conference on*, pages 2404–2409. IEEE, 2008.

[19] Meysar Zeinali and Amir Khajepour. Design and application of chattering-free sliding mode controller to cable-driven parallel robot manipulator: Theory and experiment. In *ASME 2010 International Design Engineering Technical Conferences and Computers and Information in Engineering Conference*, pages 319–327. American Society of Mechanical Engineers, 2010.

[20] Hitoshi Kino, Toshiaki Yahiro, Fumiaki Takemura, and T Morizono. Adaptive position control for fully constrained parallel wire driven systems. In *Intelligent Robots and Systems, 2006 IEEE/RSJ International Conference on*, pages 79–84. IEEE, 2006.

[21] H Jamshidifar, B Fidan, G Gungor, and A Khajepour. Adaptive vibration control of a flexible cable driven parallel robot. *IFAC-PapersOnLine*, 48(3):1302–1307, 2015.

[22] Aiguo Ming and Toshiro Higuchi. Study on multiple degree-of-freedom positioning mechanism using wires. i: Concept, design and control. *International Journal of the Japan Society for Precision Engineering*, 28(2):131–138, 1994.

[23] Daniel E Whitney. Resolved motion rate control of manipulators and human prostheses. *IEEE Transactions on man-machine systems*, 1969.

[24] Mahir Hassan and Amir Khajepour. Optimization of actuator forces in cable-based parallel manipulators using convex analysis. *Robotics, IEEE Transactions on*, 24(3):736–740, 2008.

[25] Sergio Torres-Mendez and Amir Khajepour. Analysis of a high stiffness warehousing cable-based robot. In *ASME 2014 International Design Engineering Technical Conferences and Computers and Information in Engineering Conference*, pages V05AT08A088–V05AT08A088. American Society of Mechanical Engineers, 2014.

[26] Jinghai Sun, Rendong Nan, Wenbai Zhu, Hans J Kärcher, and Hui Li. Simulation model of fast focus cabin for pointing accuracy analysis. In *SPIE Astronomical Telescopes+ Instrumentation*, pages 70171L–70171L. International Society for Optics and Photonics, 2008.

[27] Hamid D Taghirad and Meyer A Nahon. Dynamic analysis of a macro–micro redundantly actuated parallel manipulator. *Advanced Robotics*, 22(9):949–981, 2008.

[28] Ren Gexue, Lu Qiuhai, Hu Ning, Nan Rendong, and Peng Bo. On vibration control with stewart parallel mechanism. *Mechatronics*, 14(1):1–13, 2004.

[29] So-Ryeok Oh and Sunil K Agrawal. Cable suspended planar robots with redundant cables: controllers with positive tensions. *Robotics, IEEE Transactions on*, 21(3):457–465, 2005.

[30] Abbas Fattah and Sunil K Agrawal. On the design of cable-suspended planar parallel robots. *Journal of mechanical design*, 127(5):1021–1028, 2005.

[31] Robert L Williams and Paolo Gallina. Planar cable-direct-driven robots: design for wrench exertion. *Journal of intelligent and robotic systems*, 35(2):203–219, 2002.

[32] Sergio Javier Torres Mendez. Low mobility cable robot with application to robotic warehousing. 2014.

[33] Xavier Weber, Loic Cuvillon, and Jacques Gangloff. Active vibration canceling of a cable-driven parallel robot using reaction wheels. In *Intelligent Robots and Systems (IROS 2014), 2014 IEEE/RSJ International Conference on*, pages 1724–1729. IEEE, 2014.

[34] Mitchell Rushton and Amir Khajepour. Optimal actuator placement for vibration control of a planar cable-driven robotic manipulator. In *2016 American Control Conference (ACC)*, pages 3020–3025. IEEE, 2016.

[35] Claudio Melchiorri. Trajectory planning for robot manipulators. Lecture Slides.

[36] W Wang, J Yi, D Zhao, and D Liu. Design of a stable sliding-mode controller for a class of second-order underactuated systems. *IEE Proceedings-Control Theory and Applications*, 151(6):683–690, 2004.

[37] Mun-Soo Park and Dongkyoung Chwa. Swing-up and stabilization control of inverted-pendulum systems via coupled sliding-mode control method. *IEEE Transactions on Industrial Electronics*, 56(9):3541–3555, 2009.

[38] Arie Levant. Robust exact differentiation via sliding mode technique. *Automatica*, 34(3):379–384, 1998.

[39] Arie Levant. Higher-order sliding modes, differentiation and output-feedback control. *International journal of Control*, 76(9-10):924–941, 2003.

Appendices

Appendix A

Matlab Code for Model Generation

Initialize Workspace

```
clear; clc;
totaltime = 0;
```

Mechanism Parameters

```
% number of cables
n = 12;

% Box Dimensions (meters)
w_b = 0.365 ;
h_b = 0.096 ;
d_b = 0.13 ;

% Frame Dimensions (meters)
w_f = 3.16 ;
h_f = 1 ;
d_f = 0.13 ;
```

```
% % Box Anchor Points for Cables
r  = zeros(3,n);

r(:,1) = [ 5 + 10.25, 4.8, 6.5]  * 0.01;
r(:,2) = [ 5 + 18.25, -4.8, 0]   * 0.01;
r(:,3) = [ 5 + 17.25, -1.7, 8.75] * 0.01;
r(:,4) = [ -5 - 17.25, -1.7, 8.75] * 0.01;
r(:,5) = [ -5 - 18.25, -4.8, 0]  * 0.01;
r(:,6) = [ -5 - 10.25, 4.8, 6.5] * 0.01;

r(:,7:12) = r(:,1:6);
r(3,7:12) = r(3,1:6) * -1;

% Frame Anchor Points for Cables
b = zeros(3,n);

b(:,1) = [ 1.5, 0.5, 0];
b(:,2) = [ 1.58, 0.404, 0.065];
b(:,3) = [ 1.5, -0.5, 0];
b(:,4) = [ -1.5, -0.5, 0];
b(:,5) = [ -1.58, 0.404, 0.065];
b(:,6) = [ -1.5, 0.5, 0];

b(:,7:12) = b(:,1:6);
b(3,7:12) = b(3,1:6) * -1;


% Box Interial Properties
M_b = 13.7242 ; % kg
M_b = 10;
J_b = M_b/12* diag([(h_b^2+d_b^2), (w_b^2+h_b^2), (w_b^2+d_b^2)]);
```

```
% Cable Stiffnesses (N/m)
kc = 110*1000;
kc = 100;
Kc = ones(n,1) * kc;

% Actuator Properties
PendulumCount = 2;

r_pn = [ 5 + 18.25, -4.8, 0;
       -(5 + 18.25), -4.8, 0]' * 0.01;

M_pn = 0.6;
J_pn = diag([655; 483; 191]) / 1000^2;
l_pn = 0.05;
```

Model Configuration

```
exportNonlinear = false;
nonlinearExportFile = 'Xd.m';

linearise = true;
leaveLinearSymbolic = false;
exportLinear = true;
linearExportFile = 'models/SSModel_ctrb.mat';
```

State and Control Input definitions

```
tic; fprintf('Defining symbolic state variables...');

% Robot State and Inputs
syms x xd y yd z zd psi psid theta thetad phi phid real
X = [x; y; z; xd; yd; zd; psi; theta; phi; psid; thetad; phid];
```

```
syms l1 l2 l3 l4 real
u = [l1; l2; l3; l4];

% Pendulum States and Inputs
for i=1:PendulumCount,
    X(end+1) = sym(strcat('Thpn',int2str(i)));
    X(end+1) = sym(strcat('Thpn',int2str(i),'d'));
end
u = [u; sym('tau',[PendulumCount,1])];



% Final data manipulations
X = sym(X,'real'); u = sym(u,'real');
Xd = sym('Xd',[length(X(:,1)),1]);
Xd = sym(Xd,'real');

Fext = [0;0;0]; Mext = [0;0;0];

time = toc; totaltime = totaltime + time; fprintf(' %f s\n',time);
```

Rotation Matrix generation

```
%  - Frame 0: Global Frame
%  - Frame 3: Body Fixed Frame

tic; fprintf('Generating Rotation Matrices...');

% First Rotation about X Axis
R01 = [1, 0, 0;
      0, cos(psi), sin(psi);
      0, -sin(psi), cos(psi)];
% Second Rotation about Y' Axis
```

```
R12 = [cos(theta), 0, -sin(theta);
      0, 1, 0;
      sin(theta), 0, cos(theta)];
% Third Rotation about Z'' Axis
R23 = [ cos(phi), sin(phi), 0;
       -sin(phi), cos(phi), 0;
       0, 0, 1];

R03 = R23*R12*R01;
R30 = R03';

% Relate Box Angular Velocities to Euler Angle Rates
Wd = R03*[psid;0;0] + R23*R12*[0;thetad;0] + [0;0;phid];
Rr = equationsToMatrix(Wd,[psid thetad phid]);

Rr_inv = simplify(inv(Rr));

% Time derivative of Rr
Rr_d = [ -cos(theta)*sin(phi)*phid - cos(phi)*sin(theta)*thetad,
    cos(phi)*phid, 0;
          sin(phi)*sin(theta)*thetad - cos(phi)*cos(theta)*phid, -
              sin(phi)*phid, 0;
          cos(theta)*thetad, 0, 0];

time = toc; totaltime = totaltime + time; fprintf(' %f s\n',time);
```

Compute Cable Potential Energies

```
tic; fprintf('Computing Cable Potential Energies...');

% Compute Cable Lengths and Unit Vectors
for i=1:n,
    C = b(:,i) - (X(1:3)+R30*r(:,i)) ;
```

```
    l(i,1) = sqrt(C'*C);
    c(:,i) = C/l(i);
end

% Specify Initial Lengths
l0 = [u(2);u(2);u(4); u(3);u(1);u(1); u(2);u(2);u(4); u(3);u(1);u
    (1)];

% Compute Cables Tensions
for i=1:n,
   tau(i) = Kc(i).*(l(i)-l0(i)) ;
end

tau = tau';

% Compute combined potential energy
Vc = 0.5*tau'*diag(1./Kc)*tau;

time = toc; totaltime = totaltime + time; fprintf(' %f s\n',time);
```

Compute Pendulum Potential and Kinetic Energies

```
tic; fprintf('Defining Pendulum Energies');

v = [xd; yd; zd];
w = Rr * [psid; thetad; phid];

% Compute Actuator Kinetic Energies
Tpn = 0;
for i=1:PendulumCount,
    j = 2*(i-1)+13;
```

```
    % Velocity of pendulum i in inertial frame
    vpn = v + R30*( cross(w,r_pn(:,i)) + X(j+1)*l_pn*[0;sin(X(j));
        cos(X(j))] );

    % Angular Velocity of pendulum i in body frame
    wpn = [X(j+1)+w(1);w(2);w(3)];

    % Total Kinetic energy of pendulum i
    Tpn = Tpn + 0.5*M_pn*(vpn'*vpn) + 0.5*wpn'*J_pn*wpn;
end

% Compute Actuator Potential Energies
Vpn = 0;
for i=1:PendulumCount,
    j = 2*(i-1)+13;

    % height of pendulum mass from gravitational ground
    rpn = [x;y;z] + R30*( r_pn(:,i) + l_pn*[0;-cos(X(j));sin(X(j))]
        );
    hpn = rpn(2);

    % Total Potential energy of Pendulum i
    Vpn = Vpn + M_pn*9.81*hpn;
end

% Apply reactions to the Box
for i=1:PendulumCount,
    j = 4 + i ;
    Mext = Mext - [u(j);0;0];
end
```

```
time = toc; totaltime = totaltime + time; fprintf(' %f s\n',time);
```

Compute the Lagrangian

```
tic; fprintf('Computing Lagrangian...');

v = [xd; yd; zd];
w = Rr * [psid; thetad; phid];

% Compute Kinetic and Potential Energies for the Box
Tb = 0.5*M_b*(v'*v) + 0.5*w'*J_b*w;
Vb = M_b*9.81*y;

% Compute Lagrangian
L = (Tb+Tpn) - (Vb+Vc+Vpn);

time = toc; totaltime = totaltime + time; fprintf(' %f s\n',time);
```

Assemble the Nonlinear System State Equations

```
tic; fprintf('Deriving Nonlinear State Equations...');

% Translational Velocities
Xd(1:3) = [xd; yd; zd];
% Rotational Velocities
Xd(7:9) = [psid; thetad; phid];

% Actuator Velocities
NumberOfActuators = PendulumCount;
for i=1:NumberOfActuators,
    j = 2*(i-1)+13;
    Xd(j) = X(j+1);
end
```

```
% Symbolic variable setup for complex differentiations
syms t
for i=1:length(X(:,1)),
    qt(i,1) = sym(['q',num2str(i),'(t)']);
end

zero = sym('zero');
qdd = sym('qdd');

% Translational Accelerations
for i=1:3,
    zero(i) = subs(subs(diff(subs(diff(L,X(i+3)),X,qt),t),diff(qt,t)
        ,Xd),qt,X) - diff(L,X(i)) - Fext(i);
    qdd(i) = Xd(i+3);
end

% Rotational Accelerations
for i=1:3,
    zero(end+1) = subs(subs(diff(subs(diff(L,X(i+9)),X,qt),t),diff(
        qt,t),Xd),qt,X) - diff(L,X(i+6)) - Mext(i);
    qdd(end+1) = Xd(i+9);
end

% Actuator Accelerations
for i=1:NumberOfActuators,
    j = 2*(i-1)+13;
    zero(end+1) = subs(subs(diff(subs(diff(L,X(j+1)),X,qt),t),diff(
        qt,t),Xd),qt,X) - diff(L,X(j)) - u(4+i);
    qdd(end+1) = Xd(j+1);
end
```

```
% Collect and Order Equations for Second Rates
[M, F] = equationsToMatrix(zero,qdd);

M = simplify(M);

% qdd= linsolve(M,F);

qdd = inv(M)*F;

Xd(4:6) = qdd(1:3);
Xd(10:12) = qdd(4:6);

for i=1:NumberOfActuators,
    j = 2*(i-1)+13;
    Xd(j) = X(j+1);
    Xd(j+1) = qdd(6+i);
end

if exportNonlinear,
    matlabFunction(Xd,'file',nonlinearExportFile,'vars',{X,u},'
        Optimize',false);
end


time = toc; totaltime = totaltime + time; fprintf(' %f s\n',time);
```

Linearise Model

```
if linearise,
    % Specify Equilibrium Point
    X0 = zeros(length(X),1);
    X0(1) = 0;
```

```
X0(2) = 0.0;

tau0 = GenerateTensions(X0(1),X0(2),2*M_pn);
linit = subs(l,X,X0);
linit = [linit(6);linit(1);linit(4);linit(3)];
u0 = linit - tau0./kc;
u0 = [u0; zeros(NumberOfActuators,1)];

% Linearise Xd
tic; fprintf('Linearising for A');
A = jacobian(Xd,X);
time = toc; totaltime = totaltime + time; fprintf(' %f s\n',time
    );

tic; fprintf('Linearising for B');
B = jacobian(Xd,u);
time = toc; totaltime = totaltime + time; fprintf(' %f s\n',time
    );

C = eye(length(X));
D = zeros(length(X),length(u));

if leaveLinearSymbolic == false,
    tic; fprintf('Making Final Substitutions...');
    A = subs(A,[X;u],[X0;u0]);
    A = double(A);

    B = subs(B,[X;u],[X0;u0]);
    B = double(B);
    time = toc; totaltime = totaltime + time; fprintf(' %f s\n',
        time);
end
```

```
    if exportLinear,
        tic; fprintf('Exporting Linear Model...');
        save(linearExportFile,'A', 'B', 'C', 'D');
        time = toc; totaltime = totaltime + time; fprintf(' %f s\n',
            time);
    end
end

fprintf(['Done. Total Time: ',num2str(totaltime),'\n']);
```